Title
Hydrocarbon-free resonance transition 795 nm rubidium laser

Permalink
https://escholarship.org/uc/item/0pb1k5tz

Author
Wu, Sheldon Shao Quan

Publication Date
2009

Peer reviewed|Thesis/dissertation

UNIVERSITY OF CALIFORNIA, SAN DIEGO

Hydrocarbon-free resonance transition 795 nm rubidium laser

A dissertation submitted in partial satisfaction of the
requirements for the degree Doctor of Philosophy

in

Electrical Engineering (Photonics)

by

Sheldon Shao Quan Wu

Committee in charge:

Paul K.L. Yu, Chair
Raymond J. Beach
Joseph E. Ford
Yu-Hwa Lo
Thomas M. O'Neil
Clifford M. Surko

2009

The Dissertation of Sheldon Shao Quan Wu is approved, and it is

acceptable in quality and form for publication on microfilm and

electronically:

_____

_____

_____

_____

_____
Chair

University of California, San Diego

2009

TABLE OF CONTENTS

LIST OF FIGURES

LIST OF TABLES

ACKNOWLEDGEMENTS

I would like to acknowledge Professor Paul Yu for his support as the chair of my committee. His guidance over the years has proved invaluable.

I would also like to acknowledge Dr. Raymond J. Beach of Lawrence Livermore National Laboratory, without whom my present research would not exist. His support and tutelage has helped me in an immeasurable way.

Appreciation is extended to Alexander Rubenchik, Scott Mitchell, Keith Kanz, Ralph Page, Thomas Soules, Mark Rotter, and Chris Barty of LLNL for their technical support and many useful discussions. In addition, I am grateful for the Lawrence Scholar Program at LLNL for their guidance and support.

I would also like to acknowledge the Directed Energy Professional Society (DEPS) for their generous financial support during my doctoral research.

Chapter 4 contains material that has been submitted for publication as it may appear in S. S. Q. Wu, T. F. Soules, R. H. Page, S. C. Mitchell, V. Keith Kanz, R. J. Beach, Opt. Lett. 32, 2423-2425 (2007) and Optics Communications, Vol 281, 5, 1222-1225 (2008). The dissertation author was the primary investigator and author of this paper.

Chapter 6 in part is currently being prepared for submission for publication of the material. S. S. Q. Wu, A. M. Rubenchik, S. C. Mitchell, R. J. Beach. The dissertation author was the primary investigator and author of this material.

This work performed under the auspices of the U.S. Department of Energy by Lawrence Livermore National Laboratory under Contract DE-AC52-07NA27344.

VITA

2004	Bachelor of Science, University of California, San Diego
2004-2006	Research Assistant, Department of Electrical and Computer Engineering, University of California, San Diego
2006	Master of Science, University of California, San Diego
2006-2009	Lawrence Scholar, Photon Science & Applications, Lawrence Livermore National Laboratory
2009	Doctor of Philosophy, University of California, San Diego

PUBLICATIONS

G. E. Betts, W. Krzewick, S. Wu, P. K. L. Yu, "Experimental Demonstration of Linear Phase Detection," Photonics Technology Letters, IEEE , vol.19, no.13, pp.993-995, July 1, 2007

S. S. Q. Wu, T. F. Soules, R. H. Page, S. C. Mitchell, V. Keith Kanz, and R. J. Beach, "Hydrocarbon-free resonance transition 795-nm rubidium laser," Opt. Lett. 32, 2423-2425 (2007)

S. S. Q. Wu, T. F. Soules, R. H. Page, S. C. Mitchell, V. Keith Kanz, and R. J. Beach, "Resonance transition 795-nm rubidium laser using ^{3}He buffer gas", Optics Communications, Vol 281, 5, 1222-1225, 2008

S. S. Q. Wu, T. F. Soules, R. H. Page, S. C. Mitchell, V. Keith Kanz, and R. J. Beach, "Resonance transition 795-nm Rubidium laser with He buffer gas" (Invited paper), Proc. SPIE, Vol. 7005, 700523 (2008)

S. S. Wu, T. F. Soules, R. H. Page, S. C. Mitchell, V. K. Kanz, and R. J. Beach, "Developments toward a Reliable Diode-Pumped Hydrocarbon-Free 795-nm Rubidium Laser," in Conference on Lasers and Electro-Optics/Quantum Electronics and Laser Science Conference and Photonic Applications Systems Technologies, OSA Technical Digest (CD) (Optical Society of America, 2008), paper CFW5.

S. S. Q. Wu, T. F. Soules, R. H. Page, S. C. Mitchell, V. Keith Kanz, and R. J. Beach, "Hydrocarbon-free resonance transition 795-nm rubidium laser", Proc. SPIE, Vol. 6874, 68740E (2008)

S. S. Wu, T. F. Soules, R. H. Page, S. C. Mitchell, V. K. Kanz, and R. J. Beach, "Resonance Transition 795-nm Rubidium Laser Using ^{3}He Buffer Gas," in Advanced Solid-State Photonics, OSA Technical Digest Series (CD) (Optical Society of America, 2008), paper WB2.

S. S. Q. Wu, A. M. Rubenchik, S. C. Mitchell, R. J. Beach, Ionization-induced phenomena in rubidium vapor laser, Optics Express, 2009 (pending)

ABSTRACT OF THE DISSERTATION

Hydrocarbon-free resonance transition 795 nm rubidium laser

by

Sheldon Shao Quan Wu

Doctor of Philosophy

University of California, San Diego, 2009

Professor Paul K. L. Yu, Chair

Resonance transition rubidium laser operating on the $5^2P_{1/2} \rightarrow 5^2S_{1/2}$ transition
with a hydrocarbon-free buffer gas is described. An extensive conceptual and
numerical modeling study of the hydrocarbon-free rubidium laser is conducted. Prior
demonstrations of alkali resonance transition lasers have used ethane as either the

buffer gas or a buffer gas component to promote rapid fine-structure mixing. Evidence suggests that the alkali vapor reacts with the ethane producing carbon as one of the reaction products. This degrades long term laser reliability. Our experimental results with a "clean" helium-only buffer gas system pumped by a Ti:sapphire laser demonstrate all the advantages of the alkali laser, but without the reliability issues associated with the use of ethane. We further report a demonstration of a rubidium laser using a buffer gas consisting of pure ^{3}He. Using isotopically enriched ^{3}He gas yields enhanced mixing of the Rb fine-structure levels. This enables efficient lasing at reduced He buffer gas pressure, improved thermal management in high average power Rb lasers and enhanced power scaling potential of such systems. A diode-pumped alkali laser with output power of 150 W is demonstrated using commercial diode pump arrays with linewidths of ~0.5 nm, a regime requiring only modest linewidth control. We anticipate that this approach presents a new pathway to high average power lasers with good beam quality and high efficiency. Furthermore, collisional energy transfer leading to the ionization of active atoms is observed in an optically pumped Rb laser. Using a chopped Ti:sapphire laser as a pump source, their effects on the Rb laser are studied. A simple model is presented with numerical parameters gathered from published literature to explain our observations. Although these parasitic processes can strongly affect laser output, they do not appear to significantly impact the overall laser efficiency in the regime examined in this study.

Chapter 1   Introduction

1.1   High average power lasers

Many scientific, military, medical and commercial laser applications have been developed since the invention of the laser in the 1950's. Lasers with high output powers have already found central roles in a plethora of fields, including

- laser-induced nuclear fusion (e.g. National Ignition Facility at LLNL)

- detection of gravitational waves (e.g. the LIGO and LISA projects)

- laser induced breakdown spectroscopy

- laser driven particle acceleration

- directed energy (DE) applications (e.g. defensive countermeasures)

- power beaming applications (e.g. space elevator)

- atmospheric and remote sensing

- material processing (e.g. laser cutting, welding, brazing, bending)

- medical applications (e.g. surgery, laser tweezers)

The coherency, high monochromaticity, localized beam characteristics, and ability to reach extremely high powers are all properties which are desirable for many of these specialized applications. Important requirements for the practical deployment of high power lasers include compact size, light weight, high efficiency, good beam quality, high reliability, mechanical robustness through shock and vibration, and low maintenance and logistic costs.

1.1.1 Diode lasers

One of the enablers of high power lasers have been the rapid development of semiconductor gain media. Semiconductor lasers are the most compact and efficient laser available, and in fact, they far exceed gas, liquid, and solid state lasers in several of the requirements above. The maximum continuous-wave (cw) output power of a modern semiconductor laser with a 100 μm wide p-n junction is on the order of ~10 W [1]. Greater than several kilowatts of output power can be obtained using linear or two-dimensional laser diode arrays, which typically contain from several tens to several thousands of individual laser diodes.

The dramatic advantages that diode lasers offer have enabled their deployment in some military and industrial applications, but their direct use has been limited. The reason for their disfavor is in a big part due to their poor output beam quality. Diode lasers tend to have strongly astigmatic output with highly divergent beams which can not be converted to a near-diffraction-limited beam even with the use of adaptive

optics in combination with wavefront sensors. In some areas of laser material processing, such as welding and various kinds of surface treatment, beam quality is less critical because they work with larger spots, so that direct application of high-power diode lasers with poor beam quality is possible. However, a high beam quality is critically important when strong focusing of a beam with large working distance is required. Due to their inferior beam quality, roughly half of the high power diode lasers today are being used to pump solid state or fiber lasers which have better brightness, energy storage, and spectral reach than direct diode lasers.

1.1.2   Diode-pumped solid state lasers

In a diode-pumped solid state laser (DPSSL), the broadband and strongly astigmatic emission from a semiconductor laser is converted to highly coherent narrowband output ideally in the fundamental transverse mode. Advances in the manufacturing of highly efficient DPSSL's were achieved due to considerable progress in the development of highly efficient semiconductor lasers and laser arrays.

The use of narrow-band semiconductor lasers for pumping a solid state laser resulted in an order of magnitude increase in the lasing efficiency, and in a decrease in thermal loads in active elements. The high reliability and long operating life of semiconductor pump sources are attractive qualities which have allowed them to proliferate over their conventional flash lamp pumped counterparts.

The semiconductor lasers can be used for pumping a variety of solid-state lasers because absorption bands of most active media doped with rare-earth ions lie in the spectral region from 0.7 to 1.3 μm, where diode lasers are able to reach high

efficiencies. Nd:YAG laser crystals are most popular among the DPSSL active elements. Lasers based on these crystals can produce laser emission at 0.946, 1.06, 1.12, 1.3, and 1.44 μm at room temperature. The wide-spread application of Nd:YAG crystals is aided by the fact that their absorption bands are located in a spectral region that is convenient for pumping, between 0.808 and 0.812 μm.

The YAG crystals doped with other rare-earth elements have been gaining increasing importance. In particular, Yb:YAG crystals emitting at 1.029 μm with the quantum efficiency of up to 89% upon pumping at 0.97 μm are the most promising for the development of high-power cw lasers. One of the main advantages of Yb:YAG over Nd:YAG lasers is the closeness of their absorption and luminescence bands. The Yb:YAG laser emitting at 1.029 μm is pumped at 0.941 μm has 11% of the pump power converted to heat. However this value is 37% in the Nd:YAG laser pumped at 0.81 μm and emitting at 1.064 μm.

Thermal management in high power solid state lasers usually entails conductive and convective removal of heat from the gain media. Due to the geometric size and limited thermal conductivity of the media, this often poses a significant challenge. In the push to higher powers (>1kW), DPSSL's struggle to maintain near-diffraction-limited operation due to detrimental thermo-optical phenomena inherent to solid state gain media: thermally-induced focusing, stress-induced birefringence, and mechanical rupture.

The JHPSSL program at Northrop Grumman is one effort intended to develop a family of electrically powered high power solid state lasers with very good efficiency and beam quality suitable for 100 kW class directed energy applications.

1.1.3 Fiber lasers

Considerable attention has been focused on fiber-based lasers and amplifiers due to their potential for high average power combined with high efficiency, compactness, and reliability. Fiber lasers have many advantages over bulk solid state lasers. Fiber lasers are more compact, lighter, more efficient than bulk solid state lasers, and are also compatible with diode pump sources. In double-clad fiber lasers, pump conversion efficiency can be as high as 80%. Fiber lasers can have better beam quality due to mode control and thermal managements. For fiber lasers, the fiber geometry increases the surface-to-volume ratio. This makes it easier to dissipate the heat. In addition, fiber lasers are normally easier to maintain and can be operated over a long time span with high reliability. A 1 kW single-mode IPG fiber laser module operating at wavelength of 1.075 μm, excluding power supply, has a dimension of $60 \times 33 \times 5$ cm^3, weighs approximately 20 lbs, has a wall-plug efficiency of 30%, and operating lifetime of more than 10,000 hrs [2].

However, fiber laser output power remains limited by intrinsic effects such as nonlinearity and the onset of catastrophic damage. The silica damage threshold in optical fibers has been reported to be $\sim$5 W/μm^2. When the optical power inside the fiber surpasses this value, the fiber can be destroyed. Fiber facets are also highly

susceptible to optical damage. Thermal effects can still be significant in high power fiber lasers.

Nonlinear effects pose perhaps the most difficult challenges in creating high power fiber lasers. They are induced by the high power density in the small area fiber core. Among the numerous nonlinear effects, Brillouin backscattering can limit the output power of narrow-band signals and Raman scattering can generate a frequency shift which decreases the pump power and signal power.

Increasing the mode field diameter inside an active fiber is one method to increase the available output power while avoiding nonlinearity and catastrophic damage. Step index large mode area fibers can be easily fabricated with extremely large core diameters. However, this can lead to lower beam quality because of their weak guiding properties and tendency to support the propagation of higher order modes. These multimodal higher power fiber lasers have a more limited propagation range.

Dawson *et al* analyzed how thermal effects, finite pump brightness, limited doping concentrations, nonlinear optical effects and damage limit the scalability of a single aperture fiber laser [3]. He concluded that these effects interact to create hard limits on the output power of broadband fiber lasers at around 36 kW and narrowband fiber lasers at around 2 kW. Further analysis suggests that there is a practical upper limit to the scalability of the core diameter largely because a long fiber must be bent to be packaged. This in turn will limit the output power of a simple single mode, single aperture fiber laser to around 10 kW.

1.1.4   Beam combination

An alternative approach to building high-power lasers is to use arrays of relatively lower power lasers. This approach requires that the beams from the array elements being combined to have the propagation characteristics of a single beam. Technical advances have made fiber lasers a leading candidate for beam combination applications.

Historically, much of the effort to obtain good beam quality through laser beam combining has attempted to use coherent beam combination techniques. This is the analog of phased-array transmitters in the radio-frequency and microwave portions of the electromagnetic spectrum, but in the optical domain coherent beam combination has proven to be difficult because of the shortness of an optical wavelength. Coherent beam combining has been demonstrated for small arrays, but identifying robust simple phased array approaches for combining large arrays with tens to hundreds of elements with nearly ideal beam quality has been elusive.

Alternatively, high power beams can be achieved by combining individual elements with no regard to their coherency. Incoherent combining of laser beams is achieved by overlapping the individual laser beams on a target with a beam director consisting of independently controlled steering mirrors with optional adaptive optics capabilities. Compared with coherent beam combining, incoherent beam combining has the great advantage of not requiring mutual temporal coherence of the combined beams, and can be readily scaled up to a compact and reliable directed energy laser system. On the other hand, the multi-wavelength nature of the output is often

unavoidable, which may not matter for some applications while excluding others where a narrow-bandwidth output is required.

1.1.5   Chemical lasers

A completely distinct class of laser systems being considered for directed energy applications is the chemical laser. This laser obtains its energy from chemical reactions and can achieve continuous wave output with power reaching to megawatt levels. Common examples of chemical lasers are the chemical oxygen iodine laser (COIL), all gas-phase iodine laser (AGIL), the hydrogen fluoride (HF) laser and deuterium fluoride (DF) laser. The chemical oxygen-iodine laser (COIL) gained the most interest, producing radiation at 1.315 μm, and uses chlorine gas and an aqueous mixture of hydrogen peroxide and potassium hydroxide to produce excited oxygen molecules which are reacted with molecular iodine.

Megawatt class chemical lasers are being actively developed today in the Airborne Laser (ABL) and the Advanced Tactical Laser (ATL). However, the limited success of these power-scaled chemical laser systems in achieving their practical goals and the eventual realization of their logistical disadvantages has resulted in their increasing disfavor among the directed energy community. The ATL reportedly weighs in at 12000 pounds while the ABL is even heavier than that [4,5], both requiring massive airborne vehicles for deployment in the field. Add to that the requirement of monitoring and transporting substantial amount of toxic exotic fuel mix in the air makes for a frightening logistics problem. This leads to the perception that high power lasers will be a logistics burden, and that their operation will be too

complex and affected by lack of experience of operators. A high average power laser that needs no additional fuels or logistical requirements would be very attractive.

1.2   Motivations for alkali lasers

In 2002, researchers at Lawrence Livermore National Laboratory (LLNL) demonstrated a new class of laser based on diode excitation of atomic alkali vapors. The alkali laser combines the attractive beam quality and efficiency of the solid-state and fiber laser, compatibility with commercial diode pump technology, and the capability to reach high average powers without the overbearing disadvantages of the chemical laser.

1.2.1   Simplicity

Conceptually, alkali laser are one of the simplest types of lasers. The alkali vapor is itself the gain medium without any additional ion implantation or gas discharge requirements. Alkali metals are easily obtained from commercial vendors. The alkali atoms can be directly excited by the absorption of light. Because of the hydrogen-like atomic structure, their physical and spectroscopic properties are quite well-known. In fact, one of the first lasers proposed by Schawlow and Townes [6] in 1958 was based on optically pumped potassium vapor — an alkali laser!

Alkali lasers do not need large quantities of hazardous materials and can be constructed in a closed cell, eliminating the need for complicated hydrodynamic systems and discharge of chemicals. The ability to deliver high average powers in a

single aperture closed system with good beam quality highlights the conceptual simplicity of the alkali laser.

1.2.2   Compatibility with diode technology

The primary reason why it has taken so many decades for the development of the alkali laser is the lack of a suitable excitation source. Atomic transitions tend to have very narrow linewidths on the order of Å's or less, thus are extremely inefficiently excited by conventional flash lamp pump sources. Specialized lamps can be used but they are themselves highly inefficient and limited in power. Fortuitously, laser diode technology has been rapidly developing in parallel due to demand from commercial and industrial applications. Diode laser pump arrays are already replacing conventional flash lamp technology in as pump sources. As it turns out, two of the alkali metals, rubidium (Rb) and cesium (Cs), have absorption lines reachable by today's commercially available laser diode arrays. Compatibility with diode technology allows the alkali laser to share the potential efficiency advantages of diode-pumped solid state and fiber lasers.

1.2.3   Scalability

The alkali laser is a type of gas laser, which retains the advantage of ease of thermal management. As a rule, the thermal aberrations in gas laser tend to be much smaller and more manageable than those found in solid state lasers. This is in part due to the weak dependence of refractive index on gas temperature and the lack of any stress or birefringence related distortions that plague solid state media. Moreover,

much more efficient thermal extraction can be achieved in gas lasers simply by the flow the gas, a method that is unavailable for solid state media. Hence alkali lasers are less restricted by the induced thermal load and therefore can be scaled to higher powers than DPSSL's.

Moreover, the alkali lasers possess high quantum efficiencies: 95.3% for Cs, 98.1% for Rb and 99.6% for K as compared to 76% for a 1.06 μm Nd: YAG laser. High quantum efficiency is very important not only for increasing the overall laser efficiency, but also for minimizing heating problems, because the energy defect is usually converted into heat released into the gain medium.

Optically pumped gas gain medium can be scaled by increasing its volume and number of pump light sources. Hence the scaling to high power does not lead to the high optical intensity in the gain medium, such as in fiber lasers. The intensities needed in alkali lasers are comparable to those found in DPSSL's, and are insufficient in generating detrimental nonlinear effects. These and other advantages motivate the further research and development of alkali lasers.

1.3   *A short history of alkali lasers*

Coherent light amplification in optically pumped Cs vapor was first observed in 1961 by Jacobs *et al* [7]. Laser action in alkali atoms at 7.18 μm was observed in 1962 by optically pumping Cs vapor with a RF-powered helium lamp [8]. An optically pumped rubidium maser oscillating at 6835 MHz was later demonstrated in 1966 [9]. Following this, numerous theoretical and experimental studies of energy transfer, energy levels mixing and stimulated processes in the alkalis were performed

during that time. However, the alkali laser did not attract serious attention until Konefal reported in 1999 an observation of collision induced processes in rubidium-ethane vapor [10]. Konefal proposed that a longitudinally pumped alkali metal-molecular gas amplifier is theoretically possible based on his experimental studies. Konefal's laser proposal can be extended to include diode-pumping by introducing a buffer gas component such as helium that would broaden the atomic transition making it more accommodating of laser diode array linewidths. With these ideas, the concept of a diode-pumped alkali laser could finally be realized.

The first experimental demonstration of an optically pumped alkali laser in which Rb vapor in a buffer gas mixture consisting of ~70 torr of ethane and ~500 torr of He was lased under pump excitation from a Ti:sapphire laser at LLNL in 2002 [11]. Since then, several demonstrations of alkali resonance transition lasers have been reported in the scientific literature using Rb [12], Cs [13,14,15] and K [16] as the gain media. Today, several groups in the United States and abroad continue to pursue the development of the alkali laser for applications requiring high average powers and good beam quality.

There are two main approaches to developing a high average power alkali laser. One approach, following the original proposal of Konefal, relies on narrowband excitation sources and collisionally induced processes in alkali-ethane mixture to generate lasing. A notable mention is the work done by Zhdanov *et al* which used extremely line-narrowed diode arrays, $\Delta\lambda$<10 GHz, and demonstrated a 17W laser with optical-optical conversion efficiencies of 46% in Rb [17]. This approach

necessitates the development of extreme line-narrowing technology for high power diode pump arrays. Recent progress has shown that a laser diode bar incorporated in external cavity with reflecting volume Bragg grating can produce 30 W cw output power within 30 pm spectral linewidth at 780 nm [18]. Glebov *et al* predicts that a Rb vapor cell can absorb more than 85% of the emitted diode radiation. However, it is unclear whether this technology can be successfully scaled to MW power levels in the near future. At minimum, there is a significant developmental time and cost associated with such an extraordinary endeavor. Furthermore, potential chemical incompatibilities issues have already been identified in the alkali-ethane mixture used this approach.

An alternative approach, one which has been followed by Beach *et al* at LLNL, removes the need for hydrocarbons in the buffer gas and, at the same time, relaxes the requirements for the diode pump source. The approach advocates the use of relatively mature laser diode pump array technology available today. We project that in diode-pumped power scaled systems, optical to optical conversion efficiencies of >70% can be reached with a hydrocarbon-free approach using conventional laser diode arrays. The use of atmospheres of He as the buffer gas is compatible with pump linewidths of ~0.5 nm, a regime requiring only modest linewidth control with today's conventional 2-d stacks of laser diode array technology. Hydrocarbon-free diode-pumped alkali lasers present a new pathway to high average power with good beam quality and high efficiency.

Chapter 2   Physical description

2.1   Active medium

Rubidium is a soft, ductile, silvery-white metallic element of the alkali metal group. It is the fourth lightest metallic element and the sixteenth most prevalent element in the earth's crust. Rubidium is the second most electropositive and the second most alkaline element. The two isotopes of natural rubidium are ^{85}Rb (72.2%) and ^{87}Rb (27.8%). The latter is slightly radioactive, with a half-life of 49 billion years. For our purposes, the two isotopes have similar characteristics and isotopic distinctions need not be emphasized. Some selected physical and spectroscopic properties of ^{85}Rb taken from [19] are reproduced in Table 2.

The reactions of rubidium are very similar to those of other alkali metals. Rubidium burns with a violet flame in the presence of air and reacts violently with water. Rubidium also reacts vigorously with lower alcohols, halogens, oxidizing

agents, and chlorinated hydrocarbons. Rubidium metal alloys with the other alkali metals, alkaline-earth metals, antimony, bismuth, gold, and forms amalgams with mercury.

The vapor pressure of rubidium is taken from the vapor-pressure model given by [20], which is

$$\log P = 2.881 + 4.312 - \frac{4040}{T} \tag{2.1}$$

where P is the vapor pressure in torr (omit 2.881 for pressure in atmosphere), and T is the temperature in K. This model is specified to have an accuracy better than $\pm 5\%$ from 298–550K. Plots of the vapor pressure and corresponding number density are shown in Figure 2.1 and Figure 2.2, respectively.
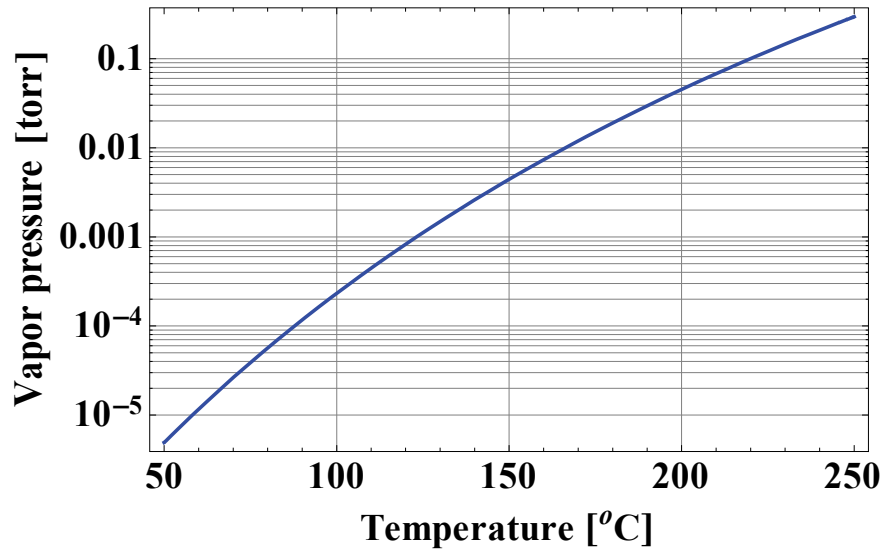
Figure 2.1: Vapor pressure of rubidium as a function of temperature
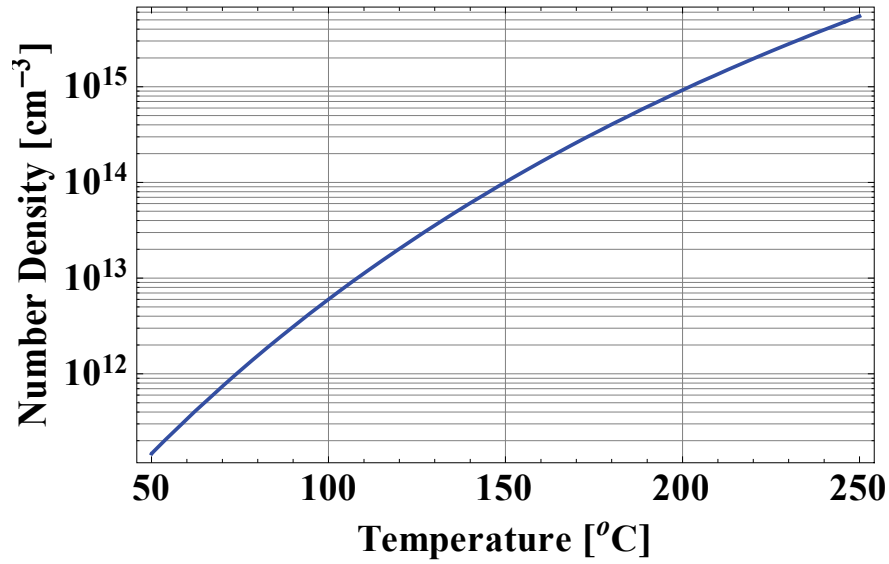
Figure 2.2: Number density of rubidium atoms in vapor form versus temperature

Rubidium has two salient optical features, commonly referred to as the D_1 and D_2 lines. The D_1 and D_2 lines are located at 795 and 780 nm respectively and can be easily accessed by a variety of light sources including commercially available laser diode arrays. Figure 2.3 shows a partial energy diagram of Rb.
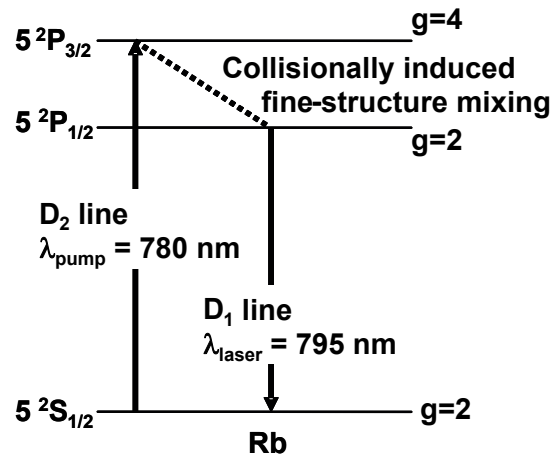
Figure 2.3: Rubidium energy level diagram. Optical gain is achieved by pumping on the D_2 transition and extracting on the D_1 transition. g denotes the degeneracy of each energy level.

Optical gain is achieved by pumping on the D_2 ($5^2S_{1/2} \rightarrow 5^2P_{3/2}$) transition and extracting on the D_1 ($5^2S_{1/2} \rightarrow 5^2P_{1/2}$) transition. While the D_1 and D_2 transitions are electric dipole transitions and possess large emission cross sections, the $5^2P_{3/2} \rightarrow 5^2P_{1/2}$ transition is not. Inelastic collisions with buffer gas atoms can provide the population transfer needed to reach inversion. Hence, to facilitate fast transfer of population between the fine-structure levels, a buffer gas is commonly added to the system.

Table 1: Relevant fundamental physical constants (2006 CODATA recommended values)

Speed of light	c	2.99792458×10^8 m/s (exact)
Planck's Constant	$\hbar$	$1.054571628(53) \times 10^{-34}$ J·s
Atomic Mass Unit	u	$1.660538782(83) \times 10^{-27}$ kg
Bohr Radius	a_0	$0.52917720859(36) \times 10^{-10}$ m
Classical Electron Radius	r_e	$2.8179402894(58) \times 10^{-15}$ m
Boltzmann's Constant	k	$1.3806504(24) \times 10^{-23}$ J/K
Loschmidt Constant	n_0	$2.6867774(47) \times 10^{25}$ m^{-3} / 1 amagat

Table 2: Rubidium-85 physical and spectroscopic properties

Atomic number	Z	37
Atomic mass	M	84.911789732(14) u
Ionization Potential	IP	4.177 126 33(10) eV
Lifetime of $5^2P_{3/2}$ state	τ_2	26.2348(77) ns
Lifetime of $5^2P_{1/2}$ state	τ_1	27.679(27) ns
D_2 ($5^2S_{1/2} \rightarrow 5^2P_{3/2}$) Wavelength (Vacuum)	λ_2	780.241368271(27) nm
D_1 ($5^2S_{1/2} \rightarrow 5^2P_{1/2}$) Wavelength (Vacuum)	λ_1	794.979014933(96) nm
D_2 ($5^2S_{1/2} \rightarrow 5^2P_{3/2}$) Transition Dipole Matrix Element	$\langle J=1/2||er||J'=3/2\rangle$	4.22753(87) e a_0
D_1 ($5^2S_{1/2} \rightarrow 5^2P_{1/2}$) Transition Dipole Matrix Element	$\langle J=1/2||er||J'=1/2\rangle$	2.9931(20) e a_0
5P Fine-structure Splitting Energy	ΔE	0.0294584 eV

2.2   Buffer gas

The theory of collision excitation and de-excitation is extremely complicated. We will follow a mostly phenomenological point of view. The processes are described by effective cross-sections, and little to no investigation of the details of the actual physical process is done. The effective cross-section can be interpreted as follows. Imagine that each atom is a hard sphere with a radius r_0 and thus a cross-

section $\sigma_{coll} = \pi r_0^2$. A collision is said to take place when the two spheres collide or touch. While for many practical applications this basic concept is quite adequate, one must keep in mind that, in reality, the range of interaction between multiple atoms is much more complex.

The collision cross-section depends on the velocity of the colliding particles. However, it is often very difficult to measure the collision cross-section as a function of the particle velocity. Hence the cross-section is usually reported in literature as a function of the average relative velocity. This is not strictly valid, but often gives a good approximation. The total rate for the collision process can then be written as $\sigma_{coll} v_{rel} N$ where N is the density of the collision partners. Under assumption of a Maxwell-Boltzmann velocity distribution, the average relative velocity v_{rel} of collision partners with masses m_1 and m_2 is

$$v_{rel} = \left[\frac{8kT}{\pi} \left(\frac{1}{m_1} + \frac{1}{m_2} \right) \right]^{\frac{1}{2}} \tag{2.2}$$

Collisions with noble gases can transfer alkali atoms from one fine-structure level to another. These collisions provide the excitation transfer mechanism to effectively mix the excited P fine-structure states. The excitation transfer maybe considered as proceeding to the follow equation

$$M(^2P_{1/2}) + X + \Delta E \leftrightarrow M(^2P_{3/2}) + X \tag{2.3}$$
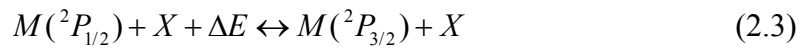
where M represents the excited alkali atom and X is the collision partner usually in its ground state. ΔE is the energy defect between the resonance substances, which is

drawn from or converted into kinetic energy of relative motion of the collision partners which equals 238 cm^{-1} for Rb.

Studies of mixing between fine-structure states in alkali atoms, induced in collisions with ground-state noble and molecular gas atoms, have been carried out by several authors [21,22,23]. Based on reported data, it is found that molecular gases such as N_2 and C_2H_6 have relatively high energy transfer cross sections for Rb fine-structure states. However, nitrogen gas also exhibits a large cross section for quenching by collisions the exciting states in Rb, in the course of which the excited atoms decay to the ground state without emitting radiation and the excitation energy is entirely converted into kinetic energy of relative motion. Since this is a highly undesirable energy loss channel, nitrogen gas is not being actively pursued as an effective buffer gas.

Ethane (C_2H_6) has been successfully shown to effectively mix the upper states in Rb and Cs and has been used in most alkali laser demonstrations to date. With a reported Rb $5^2P_{3/2} \rightarrow 5^2P_{1/2}$ energy transfer cross section of 77 Å^2 and little quenching action, it is one of the most effective gases at mixing the fine-structure levels [21]. However, one issue with this approach is the chemical reaction that takes place between the alkali and the ethane. In our previous experiments that had used ethane as a component of the buffer gas, we observed that carbonaceous deposits formed at cell surfaces (e.g. windows) that simultaneously saw high intensity pump light and were exposed to alkali vapor and ethane [12]. This negative effect has now been reported in other alkali laser demonstrations as well [24].

Helium, a commonly used buffer gas in gas dynamic lasers, has been shown to possess some of the desirable properties of ethane but without the highly undesirable reactions. Gallagher's work on collisional mixing of alkali-noble-gas systems, reproduced in Figure 2.4, shows that helium has the largest ^2P transfer cross section among all the noble gases [22]. Experimental data suggest that the alkali-noble-gas atomic interaction takes place between the noble-gas atom and the orbital electron in the alkali atom, which acts as a quasi-free particle. Beach *et al* calculated that the Rb-He fine-structure mixing cross section is sufficient to permit efficient diode-pumped Rb based systems at He buffer gas pressures of 10 atm and higher [13].
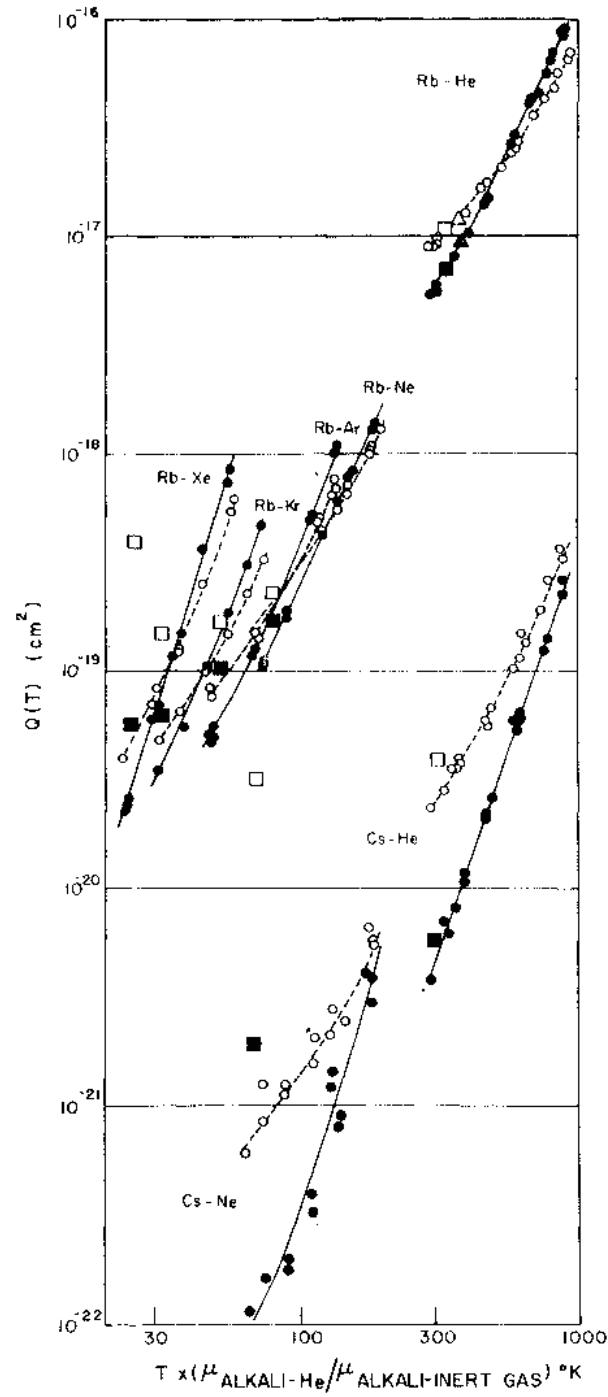
Figure 2.4: The measured alkali ^2P fine-structure excitation transfer cross sections Q(T) against reduced temperature that describes the distribution of collision velocities with various noble gases. The cross section for $^2P_{3/2} \rightarrow {}^2P_{1/2}$ are represented by broken lines and open circle points, those for $^2P_{1/2} \rightarrow {}^2P_{3/2}$ by solid lines and circles [22]. Square points represent the results quoted by Krause [25] and triangles by Beahn *et al* [26].

A secondary benefit to the use of relatively high pressure (>2 atm) helium gas in an alkali laser is the collisional broadening of the transition lines. In prior demonstrations where ethane had been used to provide the fine-structure mixing mechanism needed for lasing, helium was added to the vapor cell for collisional broadening. To better understand the reason for this, let us first discuss the situation in the absence of buffer gas.

The transition lines of a gaseous medium experience several forms of line broadening. In the regime of interest where the vapor pressure is between 10^{-4} and 10^{-2} torrs, the mechanism is dominated by Doppler broadening. In terms of the atomic mass M and the wavelength λ of the absorption line, the Doppler width at full-width at half-maximum (FWHM) is

$$\Delta \nu_D = \frac{1}{\lambda} \left(\frac{8kT}{M} \ln 2 \right)^{1/2} \tag{2.4}$$

At a temperature T=150° C, this corresponds to a FWHM linewidth of 0.6 GHz. Hence pure Rb vapor will interact with light in a very narrow spectral window of 0.6 GHz. While this can be obtained without difficulty in many types of laser sources, we are ultimately interested in using commercial diode array technology with nominal linewidths of 250 GHz or larger. Hence to increase the efficacy of this interaction, we can further increase the width of the transition lines by adding a buffer gas. By adding several atmospheres of helium gas, the transition lines are broadened to more effectively absorb the pump radiation. A summary of measured broadening data for He gas reported in [27] is found in Table 3.

Table 3: Pressure broadening data of Rb D$_1$ and D$_2$ lines by ^{3}He and ^{4}He at 353 K.

	^{4}He	^{3}He
D$_2$ full width [GHz/amg]	18.1 ± 0.2	20.8 ± 0.2
D$_2$ line shift [GHz/amg]	0.46 ± 0.06	0.68 ± 0.05
D$_1$ full width [GHz/amg]	18.0 ± 0.2	18.7 ± 0.3
D$_1$ line shift [GHz/amg]	4.3 ± 0.1	5.64 ± 0.15

The buffer gas also turns the Doppler broadened inhomogenous medium into one with a homogenous absorption feature. In an inhomogeneous atomic system, the individual atoms are distinguishable, with each atom having a unique transition frequency. The medium could be treated as made up of classes of atoms where in each class all the atoms are identical but with little interaction between the discrete classes. When the medium is homogeneously broadened, the atoms are indistinguishable and have the same transition energies. The atoms can then be treated as single spectroscopic group. This is especially helpful in the case of broadband pumping because absorption in the far wings of the transition line contributes to the central lobe instead of a single sub-class of atoms with transition energies nearby. As a result, more efficient single mode lasing operation is possible.

2.3   Vapor cell

The vapor cell contains the rubidium vapor and the buffer gas. For our initial experiments we used a custom-made ceramic cell shown in Figure 2.5.

Figure 2.5: The ceramic cell that was used in our early laser experiments

The Rb vapor and buffer gas are contained in a 3 cm long cylindrical ceramic

cell with sapphire windows that are AR coated on their external surfaces, but uncoated

on their internal surfaces. The ceramic body is connected to a niobium tube with an

industry-standard VCR® seal stainless steel gasket. The parts are vacuum-tested

before putting into operation. Due to an unanticipated event, the optic axes of the pair

of sapphire windows were set at unknown orientations. Since the windows were

already soldered on to our vapor cell, and correction would have involved breaking of

the seals and reconstruction of the cell, we chose to continue with the laser experiment

with the cells we had.

Rb was introduced into the cell as a pure metal. Due to its low melting point,

Rb can be transferred either by scooping it as a solid or drawing it into a hypodermic

needle as a liquid. This was followed by cell evacuation using a laboratory vacuum

system and then the introduction of He buffer gas at room temperature (~20° C). The

cell is then placed in a close-fit copper oven with electric heaters that allowed us to

maintain the cell temperature to within 1° C and to fix the resulting Rb saturated vapor pressure inside the cell.

For use in our later experiments, new vapor cells were created using standard vacuum parts made out of stainless steel, shown in Figure 2.6. The availability of vacuum technology means that we could fashion cells of any design of our choosing and change certain aspects as easily as swapping parts. Stainless steel was chosen as the material because of its relative chemical inertness to the alkalis. Each cell had two viewports made of sapphire held in a stainless steel fitting. Copper gaskets were used in each seal between different components.
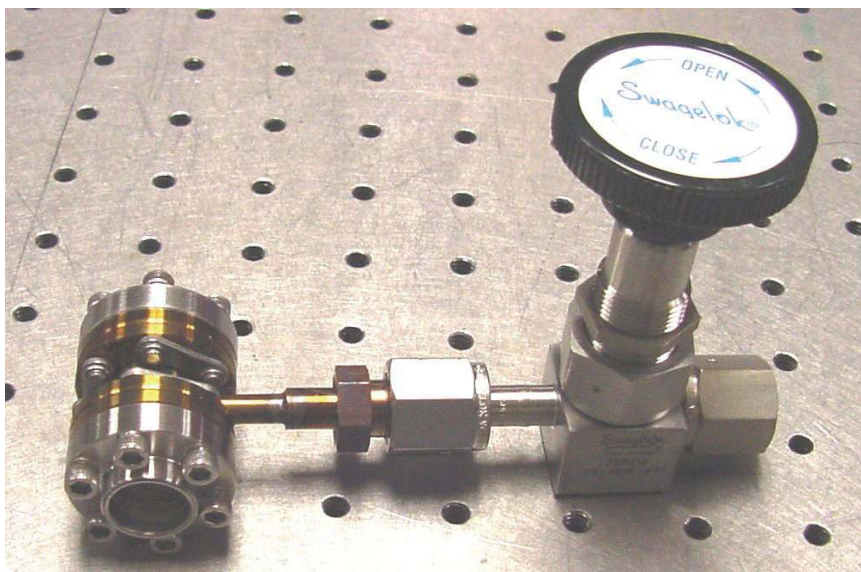
Figure 2.6: Picture of a 3 cm long stainless steel vapor cell that was used in later diode-pumped laser experiments.

2.4   Optical cavity

An optical cavity provides the necessary feedback in order for lasing to commence. Standard spherical dielectric mirrors from commercial vendors (e.g. Melles Griot, Thorlabs) with appropriate anti-reflective coatings for our wavelength

range were utilized. The complete cavity is formed by either two concave curvature mirrors or a concave and flat combination. The cavity is typically set in a near concentric configuration. The cavity length is then adjusted for best modal overlap efficiency between the pump beam and the cavity mode.

2.5   Optical excitation source

For lasing to occur in our scheme, the Rb atoms must be excited to the $5^2P_{3/2}$ state by absorption of pump radiation. A Spectra-Physics model 3900s Ti:sapphire laser was used as the excitation source in our initial low-power experiments. This laser is wavelength tunable over 760 nm - 900 nm and has a nominal linewidth of in the range of 1-9 GHz depending on the internal optical configuration. The Ti:sapphire laser is pumped by a 10 W diode-pumped neodymium vanadate laser. The maximum power available from the Ti:sapphire laser ranges from 1.9-2.7 W.
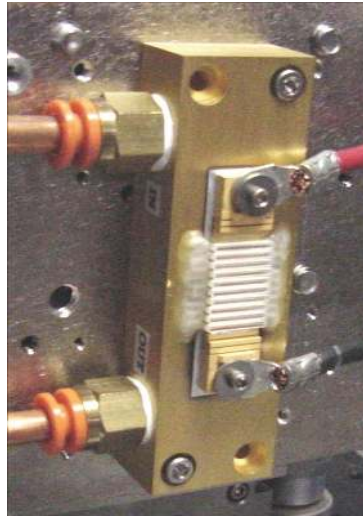
Figure 2.7: A Lasertel laser diode array used in our later experiments.

For our later experiments, diode laser arrays were used as excitation source. These semiconductor laser arrays were fabricated by Lasertel™ and one array can be seen in Figure 2.7. They are equipped with micro-optic lenses for beam collimation and low-contrast gratings for spectral control. With the added components, the nominal specifications include a 1.5×1 cm source aperture size and an angular spread of 15×150 mrad with a 0.5 nm spectral width. Each water-cooled diode array package is capable of producing 500 W of power in cw operation. The spectral characteristic of the output radiation is shown in Figure 2.8 while the spatial cross-sectional profiles are shown in Figure 2.9.
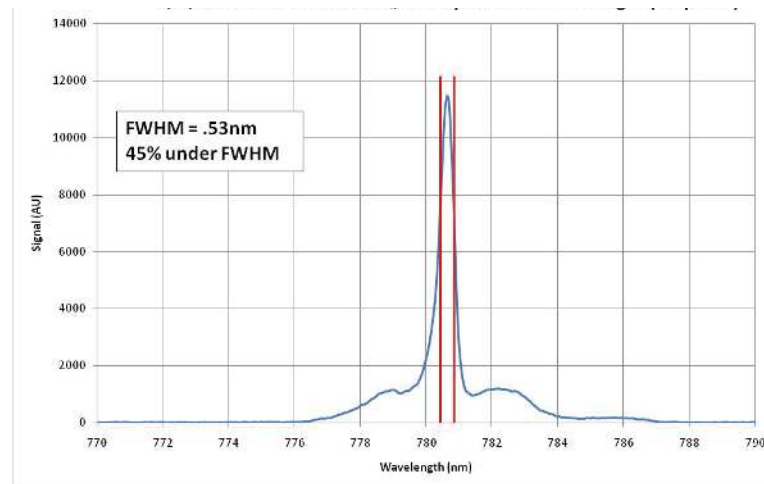
Figure 2.8: Spectral characteristics of a typical laser diode array used in our experiments.
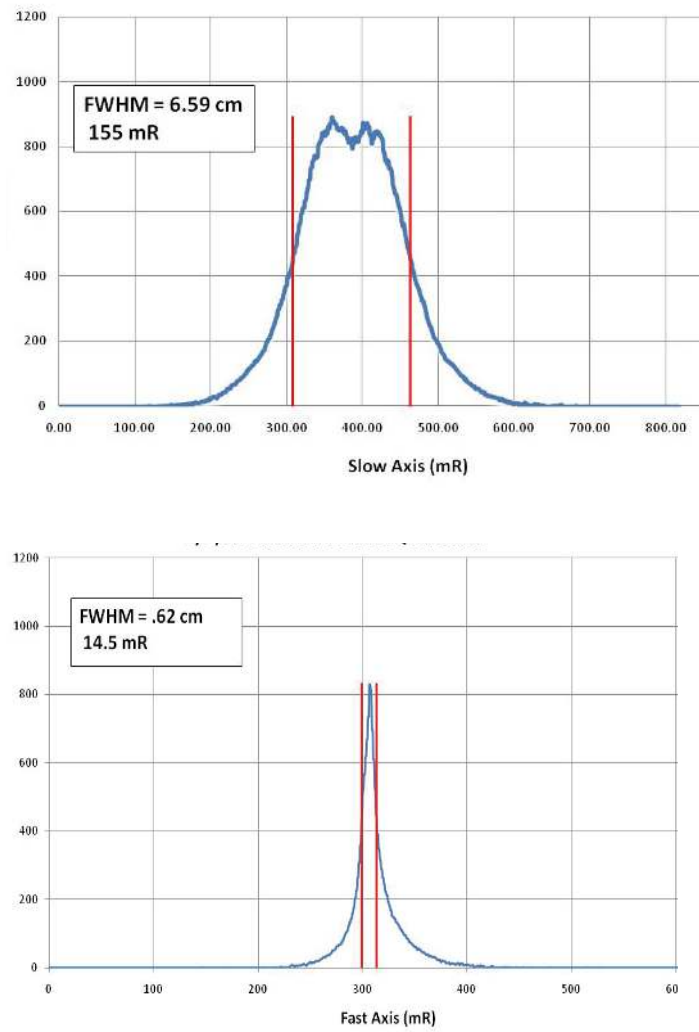
Figure 2.9: Angular spread measurement of a typical laser diode array used in our experiment. Measured data for the slow axis is shown on top and the fast axis (collimated) is shown at the bottom.

Chapter 3   Elementary theory of the laser

3.1   Method of solution

In an optically pumped laser, the gain medium absorbs energy from the pump radiation which, under optimum conditions, leads to amplification of the laser field. Hence we seek to describe the dynamics of an atomic vapor in the presence of electromagnetic fields and foreign gases. For the vast majority of problems in laser physics, Maxwell's equations with classical fields will describe the laser-atom interaction quite adequately. The atomic behavior is treated quantum mechanically while the fields are treated classically. In laser literature, this is generally referred to as the semiclassical model. The purpose of this chapter is to justify the resulting laser equations starting from the basic equations of atomic physics describing the coupled evolution of particles and the field.

3.2 Atom-field interaction

An atomic system interacting with an external electromagnetic field can be described by the minimum coupling Hamiltonian

$$H = \frac{1}{2m}\left[\mathbf{p} - e\mathbf{A}(\mathbf{r},t)\right]^2 + V(\mathbf{r}) \tag{3.1}$$

where $\mathbf{p}$ is the momentum of the electron, $\mathbf{r}$ the position of the electron, $V(\mathbf{r})$ the Coulomb potential, $\mathbf{A}(\mathbf{r},t)$ the vector potential of the field in the transverse gauge. Interaction of the electromagnetic field with the spin magnetic moment associated with the electron is usually negligible for allowed optical transitions, and thus is not considered here. We make use of a unitary transformation,

$$\left|\psi(t)\right\rangle = \exp\left[\frac{ie}{\hbar}\mathbf{r}\cdot\mathbf{A}(\mathbf{r},t)\right]\left|\phi(t)\right\rangle \tag{3.2}$$

When the wavelength of light is much longer than the size of the atom, we may apply the dipole approximation, $\mathbf{A}(\mathbf{r},t) \approx \mathbf{A}(\mathbf{R},t)$, where $\mathbf{R}$ is the position of the atom. This is a very good approximation for the alkali laser since the wavelengths of interest are close to a µm in contrast with the Å-scale atomic radius. Substituting (3.2) into the time-dependent Schrödinger's equation, $H\left|\psi(t)\right\rangle = i\hbar\frac{\partial}{\partial t}\left|\psi(t)\right\rangle$, we get,

$$\exp\left[\frac{ie}{\hbar}\mathbf{r}\cdot\mathbf{A}(\mathbf{R},t)\right]\left[\frac{p^2}{2m}+V(\mathbf{r})\right]\left|\phi(t)\right\rangle = i\hbar\exp\left[\frac{ie}{\hbar}\mathbf{r}\cdot\mathbf{A}(\mathbf{R},t)\right]\left[\frac{ie}{\hbar}\mathbf{r}\cdot\frac{\partial\mathbf{A}(\mathbf{R},t)}{\partial t}+\frac{\partial}{\partial t}\right]\left|\phi(t)\right\rangle$$

$$\tag{3.3}$$

Using $\mathbf{E}(\mathbf{R},t) = -\frac{\partial\mathbf{A}(\mathbf{R},t)}{\partial t}$, we arrive at

$$\left[\frac{p^2}{2m}+V(\mathbf{r})-e\mathbf{r}\cdot\mathbf{E}(\mathbf{R},t)\right]|\phi(t)\rangle = i\hbar\frac{\partial}{\partial t}|\phi(t)\rangle \qquad (3.4)$$

Hence the interaction Hamiltonian is simply $H_I = -e\mathbf{r}\cdot\mathbf{E}(\mathbf{R},t)$.

There has been substantial discussion over the years since Lamb first raised concerns about the use of a Hamiltonian involving **r·E** versus one involving **p·A** [28]. This has caused persistent confusion in some calculations stemming from a difference in gauges (e.g. see [29,30,31,32]). We will follow the convention set in quantum optics literature and use (3.4) for of its intuitive connection with classical physics and excellent accuracy that has been verified by experiment.

3.3   Ensembles and the density operator

There is a large population of active atoms interacting with electromagnetic fields and buffer gas atoms. As a result of frequent collisions with buffer gas atoms, the media is homogeneously broadened. In this case, the active atoms are assumed to be indistinguishable and have the same transition energies. It is intractable to attempt to solve the equation of motion of each individual active atom in the gain media. To treat this problem, we employ the master equation approach which utilizes the density operator formalism to describe the evolution of a statistical ensemble of identical particles in the presence of an external potential.

More formally, this approach allows us to describe the dynamics of an open system of interest — the alkali vapor, and to disregard the reservoir dynamics — the buffer gas and surroundings. As described in [33], consider a system where the relevant particle A interacts with a system R having a very large number of degrees of

freedom, for example the ensemble of the other particles in the gas. R can be considered as a reservoir. Then the evolution equation for A is simple if there are two distinct time scales in the problem: a very short time T_2 characterizing the fluctuations of the perturbation exerted by R on A, and a much longer time T_A characterizing the rate of variation of A. If we consider only a coarse-grained rate of variation, averaged over a time Δt such that $T_2 << \Delta t << T_A$, then simple kinetic equations can be obtained for the distribution functions of A. Mechanically, it is accomplished by tracing out the degrees of freedom of the reservoir and applying the Markov approximation. This is the essence of the master equation approach which we will accept and utilize without further justification. The interested reader is encouraged to peruse [33] for a thorough exposition on this subject.

Consider a large ensemble of independent versions of the same atomic system, each in some arbitrary quantum state $|\varphi\rangle$. The density operator is defined as

$$\rho = \sum_{\varphi} P_{\varphi} |\varphi\rangle\langle\varphi| \qquad (3.5)$$

where P_{φ} is the relative fraction of the atoms in the state $|\varphi\rangle$. Each $|\varphi\rangle$ can be expanded in the basis of eigenstates, $|\varphi\rangle = \sum_{i} c_i^{\varphi} |i\rangle$. It follows that,

$$\rho_{nm} = \sum_{\varphi} P_{\varphi} c_n^{\varphi} (c_m^{\varphi})^* \qquad (3.6)$$

Hence the diagonal elements ρ_{nn} represent the expectation value for the fraction of population found in eigenstate $|n\rangle$. The off-diagonal terms represent atomic coherence between energy levels which can be related to the dipole moment of the ensemble. The normalization and Hermitian properties of the density operator give

$$\sum_n \rho_{nn} = 1, \quad \rho_{nm} = \rho_{mn}^{*} \tag{3.7}$$

where * denotes complex conjugate. One can easily show that the equation of motion of the density operator is governed by

$$\frac{d\rho}{dt} = -\frac{i}{\hbar}[H, \rho] \tag{3.8}$$

3.4   System parameters

With the basic machinery in place, we will discuss a few important aspects of our system of interest. In the dipole approximation, the electric field is not a function of the atomic coordinates. Therefore the matrix elements for $H_I = -e\mathbf{r} \cdot \mathbf{E}(\mathbf{R}, t)$ reduce to

$$\langle n | H_I | m \rangle = -e \langle n | \mathbf{r} | m \rangle \cdot \mathbf{E}(\mathbf{R}, t) = -\boldsymbol{\mu}_{\mathbf{nm}} \cdot \mathbf{E}(\mathbf{R}, t) \tag{3.9}$$

where $\mu_{nm} = er_{nm}$ is the complex dipole moment. Furthermore, the expression (3.9) can be simplified in cases with arbitrarily polarized light and randomly aligned atoms. If the electromagnetic field is polarized along one axis, then only that component of $\langle n | \mathbf{r} | m \rangle$ is relevant, and if the atoms are randomly aligned then it is appropriate to average over the couplings. Recall that the spherical average of $cos^2\theta$ is 1/3. Therefore in this case,

$$\left\langle \left| \boldsymbol{\mu}_{\mathbf{nm}} \cdot \mathbf{E}(\mathbf{R}, t) \right|^2 \right\rangle_{\text{orientation}} = \frac{1}{3} \left| \mu_{nm} E(\mathbf{R}, t) \right|^2 \tag{3.10}$$

For convenience, we put $\mathbf{R}$ at the origin and treat the electric field as simple plane waves,

$$\mathbf{E}(\mathbf{R},t) = \mathbf{E_P} \cos(\mathbf{k} \cdot \mathbf{R} - \omega_p t) + \mathbf{E_L} \cos(\mathbf{k} \cdot \mathbf{R} - \omega_L t)$$
$$\rightarrow \mathbf{E_P} \cos(\omega_p t) + \mathbf{E_L} \cos(\omega_L t)$$

$$(3.11)$$

where the subscripts P and L refer to the pump and laser fields. $\mathbf{E_P}$ and $\mathbf{E_L}$ may be slowly varying functions of time as long as the variation is slower than all other time scales in the atomic system. One need not worry about the relative phase between the two optical fields because we will show, in the following section, that high frequency interference terms average to zero over any significant integration time and we will only be concerned with the slowly varying portion of the equations. In essence, the two fields can be effectively treated as incoherent in the same level of approximation.

The assumed plane wave nature of $\mathbf{E}(\mathbf{R},t)$ is a fairly good approximation to real laser fields. Optical outputs from many lasers are well described by Gaussian beams which behave similarly to plane waves near their beam waist. The radius of curvature of wavefronts comprising the beam is $R(z) = z\left[1 + (z_R / z)^2\right]$ where z_R is the Rayleigh range parameter. Near the beam waist, or $z < z_R$, the wavefronts can be approximated as planar. For diode laser arrays and other incoherent pump sources, the planar interaction region may be excessively short for practical reasons and thus the pump light must be ducted in a guided structure. The pump light in this case is rapidly homogenized via reflections in the duct and can be treated as propagation of a uniform incoherent image compatible with our simple field prescription.

3.5   Relaxation effects

In an atom-atom collision, the atomic energy states experience random shifts with or without an accompanied change of state. Those collisions that do not result in changes in energy state are called elastic collisions which typically occur very frequently in gas lasers on the timescale of picoseconds. Inelastic collisions, on the other hand, cause the atoms to change their energy states. A common process in gas atomic lasers is the "quenching" collision where an active atom collisionally transfers its excitation energy to a buffer gas atom and falls to a lower energy state.

The effects of dephasing perturbations such as in collisions with other atoms can be modeled as additional contributions to the decay of off-diagonal density matrix elements. Fine structure mixing and quenching collisions are included as excitation transfer processes that affect the populations of the individual energy levels.

The physical interpretation of the elements of the density matrix allows us to include in these equations rates associated with relaxation and collision processes. The decay of an atom in an excited state may be understood from a simple model where the atom is coupled to a thermal reservoir. The atomic decay rate can be derived in the Weisskopf-Wigner theory of spontaneous emission [34]. Terms due to spontaneous emission between two atomic levels are obtained for the atomic density matrix equation of motion,

$$\frac{d\rho_{22}}{dt} = -\frac{\rho_{22}}{\tau}$$

$$\frac{d\rho_{21}}{dt} = -\frac{\rho_{21}}{2\tau} \tag{3.12}$$

$$\frac{d\rho_{11}}{dt} = \frac{\rho_{22}}{\tau}$$

Here τ represent the radiative lifetime of the excited state. Collisional energy transfer can be modeled in the same way by replacing $1/\tau$ with a collisional excitation transfer rate γ.

The off-diagonal elements which represent coherence between states decay rapidly with collisions with buffer gas atoms. This is due to the fact that the phase of the radiating atomic dipole is shifted in a somewhat random fashion, and the contributions of such a collection tend to zero over a time period long compared to the time between collisions. A simplistic way to model collisional damping effects is to include decay terms in the density matrix equations,

$$\frac{d\rho_{nm}}{dt} = -\Gamma_{nm}^{(elastic)}\rho_{nm}, \quad (n \neq m) \tag{3.13}$$

where Γ, sometimes written as $1/T_2$ in literature, represent the rate of decoherence due to elastic collisions with buffer gas atoms. Hence the total decoherence rate can be written as

$$\Gamma_{nm} = \Gamma_{nm}^{(elastic)} + \frac{1}{2}\left(\frac{1}{\tau} + \gamma^{(inelastic)}\right) \tag{3.14}$$

The decoherence rate due to elastic collisions is typically many orders of magnitude larger than the spontaneous emission and inelastic collision rates. Thus, to a good approximation in our system,

$$\Gamma_{nm} \approx \Gamma_{nm}^{(elastic)} \gg \frac{1}{2}\left(\frac{1}{\tau}+\gamma^{(inelastic)}\right) \tag{3.15}$$

3.6   Formulation of atomic equations

Starting from the definition of the density operator (3.8), the evolution of the atomic vapor system and its interaction with the electromagnetic fields with the inclusion of energy transfer and decoherence terms is described by

$$\frac{d\rho_{nn}}{dt} + \sum_m \frac{\rho_{mm}}{\tau_m} = -\frac{i}{\hbar}\sum_k (H_{nk}\rho_{kn} - \rho_{nk}H_{kn})$$

$$\frac{d\rho_{nm}}{dt} + \Gamma_{nm}\rho_{nm} = -\frac{i}{\hbar}\sum_k (H_{nk}\rho_{km} - \rho_{nk}H_{km}) \tag{3.16}$$

Energy transfer processes independent of the driving fields are symbolically

represented by $\sum_m \frac{\rho_{mm}}{\tau_m}$. They may include spontaneous emission, fine-structure

mixing, quenching collisions, etc. We will designate the ground state $5^2S_{1/2}$ as state $|1\rangle$

and the excited states $5^2P_{1/2}$ and $5^2P_{1/2}$ as states $|2\rangle$ and $|3\rangle$, respectively. Inserting the

definition of H_{nm},

$$\frac{d\rho_{33}}{dt} + \sum_m \frac{\rho_{mm}}{\tau_m} = \frac{i}{\hbar}(\boldsymbol{\mu_{13}}^*\rho_{13} - \boldsymbol{\mu_{13}}\rho_{13}^*)\cdot\mathbf{E}(t)$$

$$\frac{d\rho_{22}}{dt} + \sum_m \frac{\rho_{mm}}{\tau_m} = \frac{i}{\hbar}(\boldsymbol{\mu_{21}}\rho_{21}^* - \boldsymbol{\mu_{21}}^*\rho_{21})\cdot\mathbf{E}(t) \tag{3.17}$$

$$\frac{d\rho_{11}}{dt} + \sum_m \frac{\rho_{mm}}{\tau_m} = \frac{i}{\hbar}(\boldsymbol{\mu_{21}}^*\rho_{21} - \boldsymbol{\mu_{21}}\rho_{21}^* + \boldsymbol{\mu_{13}}\rho_{13}^* - \boldsymbol{\mu_{13}}^*\rho_{13})\cdot\mathbf{E}(t)$$

The corresponding coherence (off-diagonal) terms are

$$\frac{d\rho_{21}}{dt} + \Gamma_{21}\rho_{21} = -i\omega_{21}\rho_{21} + \frac{i}{\hbar}\boldsymbol{\mu_{21}} \cdot \mathbf{E}(t)(\rho_{11} - \rho_{22}) - \frac{i}{\hbar}\boldsymbol{\mu_{13}}^* \cdot \mathbf{E}(t)\rho_{23}$$

$$\frac{d\rho_{13}}{dt} + \Gamma_{13}\rho_{13} = i\omega_{31}\rho_{13} + \frac{i}{\hbar}\boldsymbol{\mu_{13}} \cdot \mathbf{E}(t)(\rho_{33} - \rho_{11}) + \frac{i}{\hbar}\boldsymbol{\mu_{21}}^* \cdot \mathbf{E}(t)\rho_{23} \qquad (3.18)$$

$$\frac{d\rho_{23}}{dt} + \Gamma_{23}\rho_{23} = i(\omega_{31} - \omega_{21})\rho_{23} + \frac{i}{\hbar}\boldsymbol{\mu_{21}} \cdot \mathbf{E}(t)\rho_{13} - \frac{i}{\hbar}\boldsymbol{\mu_{13}} \cdot \mathbf{E}(t)\rho_{21}$$

where $\omega_{21} = \dfrac{E_2 - E_1}{\hbar}$ and $\omega_{31} = \dfrac{E_3 - E_1}{\hbar}$ are the resonance transition frequencies for the

D_1 and D_2 absorption lines, respectively. Observe that each off-diagonal term

oscillates at optical frequencies. Let us introduce

$$\rho_{21} = \sigma_{21}e^{-i\omega_L t}$$
$$\rho_{13} = \sigma_{13}e^{i\omega_P t} \qquad (3.19)$$
$$\rho_{23} = \sigma_{23}e^{i(\omega_P - \omega_L)t}$$

where σ's represents the slowly-varying envelope of the rapidly oscillating atomic

coherence. The full expression for σ_{21} is

$$\frac{d\sigma_{21}}{dt} = \frac{i\boldsymbol{\mu_{21}}}{2\hbar} \cdot \left(\mathbf{E_L} + \mathbf{E_P}e^{i(\omega_L - \omega_P)t} + \mathbf{E_P}^*e^{i(\omega_L + \omega_P)t} + \mathbf{E_L}^*e^{i2\omega_L t}\right)(\rho_{11} - \rho_{22})$$

$$- \frac{i\boldsymbol{\mu_{13}}^*}{2\hbar} \cdot \left(\mathbf{E_P} + \mathbf{E_L}e^{i(\omega_P - \omega_L)t} + \mathbf{E_L}^*e^{i(\omega_L + \omega_P)t} + \mathbf{E_P}^*e^{i2\omega_P t}\right)\sigma_{23} \qquad (3.20)$$

$$+ i(\omega_L - \omega_{21} + i\Gamma_{21})\sigma_{21}$$

In each of the first two terms on the right, there are factors that oscillate at

optical frequencies and ones that do not. Optical frequency oscillatory terms quickly

average to zero over any appreciable time of interest and therefore can be ignored

while keeping only the slowly varying ones. By discarding the part of the

electromagnetic field that does not lead to a resonant behavior, we have invoked the

rotating wave approximation (RWA). Under this approximation, we lose certain

physical effects, such as Bloch-Siegert shift of the resonance frequency and multiwave

interactions [35]. Applying the same approximation to σ_{13} and σ_{23} and defining the

Rabi frequencies $\Omega_{21} = \dfrac{\boldsymbol{\mu_{21}} \cdot \mathbf{E_L}}{\hbar}$ and $\Omega_{13} = \dfrac{\boldsymbol{\mu_{13}} \cdot \mathbf{E_P}^*}{\hbar}$, we get

$$\frac{d\sigma_{21}}{dt} = i(\omega_L - \omega_{21} + i\Gamma_{21})\sigma_{21} + i\Omega_{21}(\rho_{11} - \rho_{22}) - i\Omega_{13}^{*}\sigma_{23}$$

$$\frac{d\sigma_{13}}{dt} = i(\omega_{31} - \omega_P + i\Gamma_{13})\sigma_{13} + i\Omega_{13}(\rho_{33} - \rho_{11}) + i\Omega_{21}^{*}\sigma_{23} \qquad (3.21)$$

$$\frac{d\sigma_{23}}{dt} = i(\omega_L - \omega_{21} + \omega_{31} - \omega_P + i\Gamma_{23})\sigma_{23} + i\Omega_{21}\sigma_{13} - i\Omega_{13}\sigma_{21}$$

Similarly for diagonal terms under the rotating wave approximation,

$$\frac{d\rho_{33}}{dt} + \sum_m \frac{\rho_{mm}}{\tau_m} = \frac{i}{2}(\Omega_{13}^{*}\sigma_{13} - \Omega_{13}\sigma_{13}^{*})$$

$$\frac{d\rho_{22}}{dt} + \sum_m \frac{\rho_{mm}}{\tau_m} = \frac{i}{2}(\Omega_{21}\sigma_{21}^{*} - \Omega_{21}^{*}\sigma_{21}) \qquad (3.22)$$

$$\frac{d\rho_{11}}{dt} + \sum_m \frac{\rho_{mm}}{\tau_m} = \frac{i}{2}(\Omega_{21}^{*}\sigma_{21} - \Omega_{21}\sigma_{21}^{*} + \Omega_{13}\sigma_{13}^{*} - \Omega_{13}^{*}\sigma_{13})$$

In alkali lasers and many other atomic systems, the decoherence rate is

typically many orders of magnitude faster than the population transfer rates, $\Gamma \gg \dfrac{1}{\tau}$.

The atomic coherence reach quasi-stationary state well before any significant change

in the populations takes place. We can apply adiabatic elimination by setting all

coherence terms to their steady states values. For adiabatic elimination of variables to

be warranted, it is necessary to have coefficients that are very different in magnitude.

As a result, variables can be separated in two groups: "fast" variables and "slow" ones.

The fast variables are able to reach the quasi-stationary values determined by

instantaneous values of the slow variables and to keep track of evolution of the latter.

Adiabatic elimination is applied in (3.21) by setting all coherence terms to the steady state, $\dfrac{d\sigma}{dt} = 0$. In this limit, we can express the atomic coherence in terms of the diagonal elements,

$$\sigma_{21} = \frac{\Omega_{21}}{2(\omega_L - \omega_{21} + i\Gamma_{21})}\left[\begin{array}{l} (\rho_{22} - \rho_{11}) \\ + \dfrac{|\Omega_{13}|^2 (\rho_{33} - \rho_{11})}{4(\omega_{31} - \omega_P + i\Gamma_{13})(\omega_L - \omega_{21} + \omega_{31} - \omega_P + i\Gamma_{23})} \end{array} \right]$$

$$\sigma_{13} = \frac{\Omega_{13}}{2(\omega_{31} - \omega_P + i\Gamma_{13})}\left[\begin{array}{l} (\rho_{11} - \rho_{33}) \\ + \dfrac{|\Omega_{21}|^2 (\rho_{11} - \rho_{22})}{4(\omega_L - \omega_{21} + i\Gamma_{21})(\omega_L - \omega_{21} + \omega_{31} - \omega_P + i\Gamma_{23})} \\ + \dfrac{|\Omega_{21}|^2 (\rho_{11} - \rho_{33})}{4(\omega_{31} - \omega_P + i\Gamma_{13})(\omega_L - \omega_{21} + \omega_{31} - \omega_P + i\Gamma_{23})} \end{array} \right] \quad (3.23)$$

$$\sigma_{23} = \frac{\Omega_{21}\Omega_{13}}{4(\omega_L - \omega_{21} + \omega_{31} - \omega_P + i\Gamma_{23})}\left(\frac{\rho_{22} - \rho_{11}}{\omega_L - \omega_{21} + i\Gamma_{21}} + \frac{\rho_{33} - \rho_{11}}{\omega_{31} - \omega_P + i\Gamma_{13}} \right)$$

An additional approximation is frequently valid in quasi-cw lasers. In the limit that each Rabi frequency is much lower than the decoherence rate, or $|\Omega|^2 \ll \Delta\omega^2 + \Gamma^2$, these equations can be expressed in powers of a small parameter

$$\xi = \left| \frac{\Omega}{2(\Delta\omega + i\Gamma)} \right| = \frac{|\Omega|}{2(\Delta\omega^2 + \Gamma^2)^{1/2}},$$

$$\sigma_{21} = \frac{\Omega_{21}(\rho_{22} - \rho_{11})}{2(\omega_L - \omega_{21} + i\Gamma_{21})} + O(\xi^3)$$

$$\sigma_{13} = \frac{\Omega_{13}(\rho_{11} - \rho_{33})}{2(\omega_{31} - \omega_P + i\Gamma_{13})} + O(\xi^3) \quad (3.24)$$

$$\sigma_{23} = O(\xi^2)$$

We will retain only the terms linear in ξ and drop all higher order terms. It suffices to note that σ_{23} is second order in ξ because σ_{23} is unimportant in the remaining calculations. This approximation is justified when the collisional relaxation rate is large, because the coherences are quickly damped away. Since the Rabi frequency is proportional to the electric field strength, this approximation may potentially break down at high optical intensities such as those found in pulsed lasers. However, at an intensity of 10 kW/cm^2 and 3 atm of He buffer gas, we find that $\xi^2 \approx$ 0.07 at resonance ($\Delta\omega = 0$). Since the neglected terms are reduced by this factor, we can safely drop them in favor of the first order terms. This simplification is also valid in the case of incoherent (broadband) excitation, since there the dipole is driven by a wide range of frequencies, and thus the dephasing between the different frequency components mimics fast damping. Substituting (3.24) into (3.22), we obtain,

$$\frac{d\rho_{33}}{dt} + \sum_m \frac{\rho_{mm}}{\tau_m} = \frac{|\Omega_{13}|^2 \, \Gamma_{13}(\rho_{11} - \rho_{33})}{2\left[(\omega_P - w_{31})^2 + \Gamma_{13}^2\right]}$$

$$\frac{d\rho_{22}}{dt} + \sum_m \frac{\rho_{mm}}{\tau_m} = \frac{|\Omega_{21}|^2 \, \Gamma_{21}(\rho_{11} - \rho_{22})}{2\left[(\omega_L - w_{21})^2 + \Gamma_{21}^2\right]} \tag{3.25}$$

$$\frac{d\rho_{11}}{dt} + \sum_m \frac{\rho_{mm}}{\tau_m} = -\frac{|\Omega_{21}|^2 \, \Gamma_{21}(\rho_{11} - \rho_{22})}{2\left[(\omega_L - w_{21})^2 + \Gamma_{21}^2\right]} - \frac{|\Omega_{13}|^2 \, \Gamma_{13}(\rho_{11} - \rho_{33})}{2\left[(\omega_P - w_{31})^2 + \Gamma_{13}^2\right]}$$

The density matrix evolution equations have now been reduced to the form of conventional rate equations. Each term on the right hand side of the equations represent optically-induced transition rates due to the pump and lasing fields. Note that when the atoms are randomly aligned with respect to the fields, orientation

averaging results in an additional factor of 1/3 in each term on the right side of the equations.

3.7 Rate equations

One can see that the rate equation limit is the end product of a series of approximations including the dipole approximation, the rotating wave approximation, adiabatic elimination, and rapid damping of coherence effects. From this point on, we can comfortably work in the rate equation limit as long as all the assumptions are satisfied.

The absorption cross section is defined as the energy absorption rate by the atom divided by the energy flux of the interacting electromagnetic field. The absorption cross section can be identified from (3.25) as

$$
\begin{aligned}
\sigma_{abs}(\omega) &= \frac{\hbar\omega|\Omega|^2}{\frac{1}{2}c\varepsilon_0|E|^2}\frac{\Gamma/2}{(\omega_0-\omega)^2+\Gamma^2}\\
&= \frac{1}{3}\frac{|\mu|^2\,\omega}{\hbar c\varepsilon_0}\frac{\Gamma}{(\omega_0-\omega)^2+\Gamma^2}
\end{aligned}
\tag{3.26}
$$

where the factor of 1/3 has been reintroduced as a result of orientation averaging. σ_{abs} is not to be confused with the slowly varying atomic coherence represented by a similar symbol. Close to resonance, the spectroscopic lineshape is nearly described by a Lorentzian function with a full-width at half-maximum (FWHM) of $\Delta v = \Gamma/\pi$.

To reduce notation in the final equations, let $n_1 = n_0\,\rho_{11}$, $n_2 = n_0\,\rho_{22}$, and $n_3 = n_0\,\rho_{33}$ where n_0 is the saturated alkali vapor density. Inserting degeneracy factors which have been neglected thus far by replacing *(n_1 - n_3)* by *(n_1 - n_3/2)*, and

substituting the incoherent population transfer rates due to collisional energy transfer
and spontaneous emission, we arrive at

$$\frac{dn_3}{dt} = \frac{\sigma_2 I_P}{\hbar \omega_P}(n_1 - \tfrac{n_3}{2}) - \gamma_{{}^2P_{3/2} \rightarrow {}^2P_{1/2}} n_3 + \gamma_{{}^2P_{1/2} \rightarrow {}^2P_{3/2}} n_2 - \frac{n_3}{\tau_2}$$

$$\frac{dn_2}{dt} = -\frac{\sigma_1 I_L}{\hbar \omega_L}(n_2 - n_1) + \gamma_{{}^2P_{3/2} \rightarrow {}^2P_{1/2}} n_3 - \gamma_{{}^2P_{1/2} \rightarrow {}^2P_{3/2}} n_2 - \frac{n_2}{\tau_1} \qquad (3.27)$$

$$\frac{dn_1}{dt} = \frac{\sigma_1 I_L}{\hbar \omega_L}(n_2 - n_1) - \frac{\sigma_2 I_P}{\hbar \omega_P}(n_1 - \tfrac{n_3}{2}) + \frac{n_2}{\tau_1} + \frac{n_3}{\tau_2}$$

where $\sigma_{1,2}$ is the $D_{1,2}$ line absorption cross section and $\tau_{1,2}$ the corresponding radiative
lifetime. I_P and I_L are the local pump and laser intensities.

Thus far we have assumed the absorption of monochromatic light (in the
RWA) that is nearly resonant with the atomic transition frequency. We can generalize
the transition rate so that it applies to broadband (incoherent) radiation. When a
continuous band of frequencies contributes to the transition rate, then the intensity I_P
must be identified with $I_P(\lambda)d\lambda$ where $I_P(\lambda)$ is the spectrally-resolved pump intensity.
The total transition rate is then found by integrating over all wavelengths in the pump
spectrum.

3.8   Field propagation in atomic media

We have derived how the applied field induces coherences and transitions in
the atomic system. If the analysis is to be self-consistent, one must also consider the
effect of the induced atomic dipole back on the field.

The source-free electromagnetic wave equation in a dielectric medium is

$$\nabla^2 \mathbf{E} - \frac{1}{c^2}\frac{\partial^2 \mathbf{E}}{\partial t^2} = \frac{1}{\varepsilon_0 c^2}\frac{\partial^2 \mathbf{P}}{\partial t^2} \tag{3.28}$$

The macroscopic polarization of the medium, $\mathbf{P}(\mathbf{R}, t)$, induced by the electric field is given by the expectation value of the dipole moment of all the atoms at position z and time t,

$$
\begin{aligned}
\mathbf{P}(\mathbf{R},t) &= n_0 \langle \mathbf{\mu} \rangle \\
&= n_0 \left[\mathbf{\mu_{21}}^* \sigma_{21}(t)e^{i(kz-\omega t)} + \mathbf{\mu_{21}}\sigma_{21}^*(t)e^{-i(kz-\omega t)} \right] \\
&= 2n_0 \, \mathrm{Re}\left[\mathbf{\mu_{21}}^* \sigma_{21}(t)e^{i(kz-\omega t)} \right]
\end{aligned}
\tag{3.29}
$$

Recall that σ_{21} is the slowly varying envelope of the atomic coherence. Now for the resonant electric field, it can be written as

$$\mathbf{E}(\mathbf{R},t) = \mathrm{Re}\left[\mathbf{E_L}(z,t)e^{i(kz-\omega t)} \right] \tag{3.30}$$

An additional assumption implied by the form assumed in (3.30) is that the field amplitude variation is also small on the timescale of both an optical period $1/\omega$ and the wavelength $1/k$. This is summarized by the inequalities,

$$\left|\frac{\partial^2 E_L}{\partial z^2}\right| \ll k\left|\frac{\partial E_L}{\partial z}\right|, \quad \left|\frac{\partial^2 E_L}{\partial t^2}\right| \ll \omega\left|\frac{\partial E_L}{\partial t}\right|, \quad \left|\frac{\partial^2 \sigma_{21}}{\partial t^2}\right| \ll \omega\left|\frac{\partial \sigma_{21}}{\partial t}\right| \ll \omega^2 |\sigma_{21}| \tag{3.31}$$

Substituting (3.29) and (3.30) into (3.28), and making use of (3.31), we obtain the following propagation equation

$$\left(\frac{\partial}{\partial z} + \frac{1}{c}\frac{\partial}{\partial t}\right)\mathbf{E_L} = \frac{in_0\omega}{\varepsilon_0 c}\mathbf{\mu_{21}}^* \sigma_{21} \tag{3.32}$$

Multiply (3.32) by $\mathbf{E_L}^*$ and add to it the complex conjugate (c.c.) of the same

equation, and recall that $\dfrac{\partial |\mathbf{E_L}|^2}{\partial z} = \mathbf{E_L}^* \cdot \dfrac{\partial \mathbf{E_L}}{\partial z} + c.c.$ Taking the adiabatic solution for σ_{21}

from (3.24), we find

$$\left(\frac{\partial}{\partial z} + \frac{1}{c} \frac{\partial}{\partial t} \right) |\mathbf{E_L}|^2 = \frac{|\boldsymbol{\mu}_{21} \cdot \mathbf{E_L}|^2}{\varepsilon_0 \hbar c} \frac{\omega}{(\omega_{21} - \omega)^2 + \Gamma^2} \Gamma(n_2 - n_1) \tag{3.33}$$

Finally, using the definition of the absorption cross section (3.26) and rewriting in

terms of the intensity $I = \frac{1}{2} c \varepsilon_0 |E|^2$, we arrive at the transport equation for a

propagating electromagnetic wave at the laser frequency in the gain medium,

$$\left(\frac{\partial}{\partial z} + \frac{1}{c} \frac{\partial}{\partial t} \right) I_L = \sigma_{abs}(n_2 - n_1) I_L \tag{3.34}$$

When $n_2 > n_1$, the energy in the field will increase at the expense of energy

stored in the medium. Usually in quasi-cw lasers, it is true that $\dfrac{\partial I}{\partial z} \gg \dfrac{1}{c} \dfrac{\partial I}{\partial t}$. Dropping

the time derivative, (3.34) then becomes $\dfrac{\partial I}{\partial z} = g(z) I(z)$, which leads to the familiar

Beer's law and optical amplification. Similar analysis can be applied to the absorption

of the pump beam. We now have all of the theoretical tools necessary to describe a

fully operational atomic vapor laser.

3.9   *Laser rate equations*

Following a methodology previously introduced for modeling end-pumped cw

quasi-three-level lasers, longitudinal averaging simplifies calculations without loss of

applicability to high gain laser media. We characterize the populations in the various

levels by their longitudinally averaged values $n_i = \dfrac{1}{l_{gain}} \int_0^{l_{gain}} n_i(z)dz$. Integrating the

population equations over the length of the cavity and using the definition of the

longitudinally averaged values, the rate equations finally become,

$$\frac{dn_3}{dt} = W_P - \gamma_{^2P_{3/2} \to ^2P_{1/2}} n_3 + \gamma_{^2P_{1/2} \to ^2P_{3/2}} n_2 - \frac{n_3}{\tau_2}$$

$$\frac{dn_2}{dt} = -W_L + \gamma_{^2P_{3/2} \to ^2P_{1/2}} n_3 - \gamma_{^2P_{1/2} \to ^2P_{3/2}} n_2 - \frac{n_2}{\tau_1} \qquad (3.35)$$

$$\frac{dn_1}{dt} = W_L - W_P + \frac{n_2}{\tau_1} + \frac{n_3}{\tau_2}$$

where the n's now represent cavity averaged quantities, and W_P and W_L are the

longitudinally averaged pump and laser transition rates.
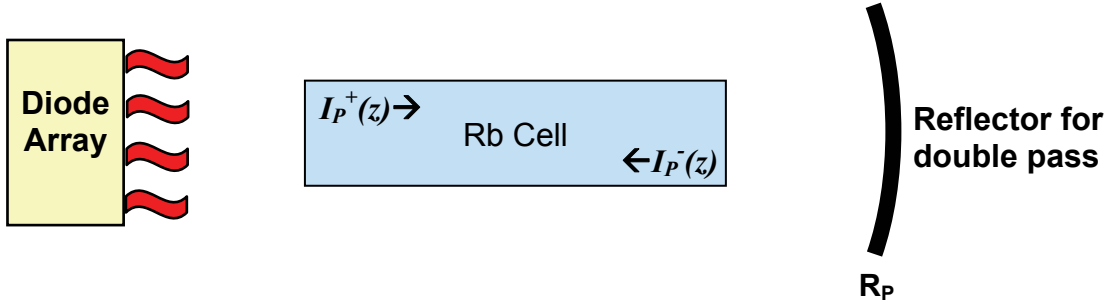
Figure 3.1: Configuration used in the calculation of the pump excitation rate. Delivery and focusing optics are not shown.

To derive the excitation rate per unit volume W_P, simply note that

$\dfrac{dI_P}{dz} = -(n_1 - \frac{n_3}{2})\sigma_2 I_P$ and observe from Figure 3.1 that

$$W_P = \frac{\eta_{del}}{V} \int d\lambda \int_{\text{laser mode}} d^3r \left(n_1 - \frac{n_3}{2} \right) \sigma_2(\lambda) \frac{I_P(\lambda)}{hc/\lambda}$$

$$= -\frac{\eta_{del}}{V} \int d\lambda \int_{\text{laser mode}} d^3r \frac{1}{hc/\lambda} \frac{dI_P}{dz}$$

$$= \frac{\eta_{del}\eta_{\text{mode}}}{l_{gain}} \int d\lambda \frac{1}{hc/\lambda} \left[I_P^+(0) - I_P^+(l_{gain}) + R_P I_P^-(l_{gain}) - R_P I_P^-(0) \right]$$

$$= \frac{\eta_{del}\eta_{\text{mode}}}{l_{gain}} \int d\lambda \frac{I_P}{hc/\lambda} \left[1 - e^{-\left(n_1 - \frac{n_3}{2} \right)\sigma_2(\lambda)l_{gain}} \right] \left[1 + R_P e^{-\left(n_1 - \frac{n_3}{2} \right)\sigma_2(\lambda)l_{gain}} \right]$$

(3.36)

where V is the total volume of the interaction region and η_{mode} is the modal overlap

factor defined as

$$\eta_{\text{mode}} = \frac{\int \Theta_L(\mathbf{r})\Theta_P(\mathbf{r})d^2\mathbf{r}}{\int \Theta_L(\mathbf{r})d^2\mathbf{r}}$$

(3.37)

and Θ's are the spatial mode intensity profiles.
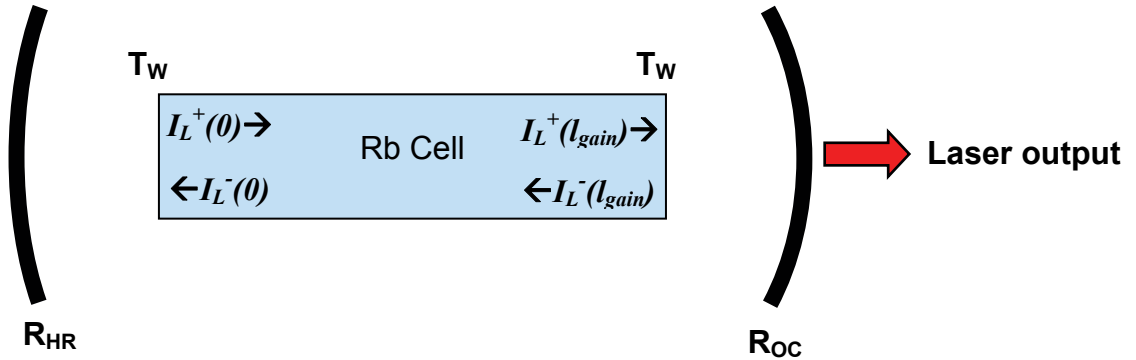
Figure 3.2: Configuration used in the calculation of laser extraction rate. I's are the intracavity laser intensities inside the gain medium. T_w represents the single-pass window transmission efficiency.

For the laser extraction rate, we start with how the laser intensity changes with

propagation length inside the laser cavity shown in Figure 3.2. From the propagation

equations,

$$\frac{dI_L^+}{dz} = (n_2 - n_1)\sigma_1 I_L^+$$

$$\frac{dI_L^-}{dz} = -(n_2 - n_1)\sigma_1 I_L^-$$

(3.38)

Therefore $I_L^+(z)I_L^-(z)$ is a constant over the length of the gain region, neglecting

diffraction. Using this along with

$$I_L^+(0) = R_{HR}T_w^2 I_L^-(0)$$

$$I_L^-(l_{gain}) = R_{OC}T_w^2 I_L^+(l_{gain})$$

(3.39)

one can immediately show

$$I_L^+(0) = T_w^2 \sqrt{R_{OC}R_{HR}} I_L^+(l_{gain})$$

$$I_L^-(0) = \sqrt{\frac{R_{OC}}{R_{HR}}} I_L^+(l_{gain})$$

(3.40)

The laser transition rate per unit volume is then,

$$W_L = \frac{1}{V}\int_{\text{laser mode}} d^3r(n_2 - n_1)\sigma_1 \frac{I_L^+ + I_L^-}{hc/\lambda_1}$$

$$= \frac{1}{V}\frac{1}{hc/\lambda_1}\int_{\text{laser mode}} d^3r\left(\frac{dI_L^+}{dz} - \frac{dI_L^-}{dz}\right)$$

$$= \frac{1}{l_{gain}}\frac{1}{hc/\lambda_1}\left[I_L^+(l_{gain}) - I_L^+(0) - I_L^-(l_{gain}) + I_L^-(0)\right]$$

(3.41)

Substituting in (3.39) and (3.40), then rewriting intracavity quantities in terms of the

output laser power using $I_L = T_w(1 - R_{OC})I^+(l_{gain})$, we arrive at

$$W_L = \frac{1}{l_{gain}}\frac{I_L}{hc/\lambda_1}\frac{R_{OC}}{1 - R_{OC}}T_w\left(\frac{1}{T_w^2\sqrt{R_{OC}R_{HR}}} - 1\right)\left(1 + \sqrt{\frac{R_{HR}}{R_{OC}}}\right)$$

(3.42)

The expressions for W_P and W_L are derived assuming that stationary pump and

laser fields exist in the cavity. In other words, they are valid for time scales long

compared to the cavity round trip time. The cavity round trip time for a typical two-mirror cavity with a mirror spacing of 40 cm is 38 ns. The rate equations (3.35) are valid in the transient domain as long as the variations of interests are much slower than the atomic and cavity lifetimes.

The astute reader should recognize that we have neglected the interference between the forward and reverse traveling waves in the cavity. This is strictly incorrect since in most lasers we have standing waves rather than noninteracting traveling waves. In fact, a phenomenon called spatial hole burning can occur in standing wave lasers, where nonuniform gain saturation develops as a result of the standing wave pattern with a peak-to-peak separation of half a wavelength between "holes", or places of minimum gain. By integrating over the length of the laser gain medium, however, we have effectively averaged over the small-scale variations. Effects relating to spatial hole burning or the scattering off of the grating produced by the standing wave pattern are disregarded in the scope of this study.

3.10   Numerical modeling

The set of rate equations (3.35) with time derivatives set to zero coupled with the auxiliary conditions

$$1 = R_{HR} R_{OC} T_w^{\,4} e^{2(n_2 - n_1)\sigma_1 l_{gain}} \tag{3.43}$$

$$n_1 + n_2 + n_3 = n_0 \tag{3.44}$$

determine the steady-state operating condition of the laser. n_0 is the saturated vapor density of Rb at operating temperature. All cross sections, lifetimes and other spectroscopic parameters used in our model are based on literature reported values.

We can further reduce computation complexity of the system of equations by defining the dimensionless quantities,

$$N_i = \frac{n_i}{n_0}, \quad i = 1, 2, 3$$

$$Q_P = \left(\frac{\hbar\omega}{\sigma_2 \tau_2} \right)^{-1} I_P \tag{3.45}$$

$$Q_L = \left(\frac{\hbar\omega_L}{\sigma_1 \tau_1} \right)^{-1} I_L$$

Furthermore, using (3.43) and (3.44) we find,

$$N_{1,2} = \frac{1 - N_3}{2} \pm \frac{1}{4 n_0 \sigma_1 l_{gain}} \log\left(T_w^{\,4} R_{HR} R_{OC} \right) \tag{3.46}$$

Upon substituting (3.45) and (3.46) into (3.35),

$$0 = \tilde{W}_P - \gamma_{^2P_{3/2} \to {}^2P_{1/2}} N_3 + \gamma_{^2P_{1/2} \to {}^2P_{3/2}} N_2 - \frac{N_3}{\tau_2}$$

$$0 = -\tilde{W}_L + \gamma_{^2P_{3/2} \to {}^2P_{1/2}} N_3 - \gamma_{^2P_{1/2} \to {}^2P_{3/2}} N_2 - \frac{N_2}{\tau_1} \tag{3.47}$$

where the normalized volumetric transition rates are

$$\tilde{W}_P = \frac{\eta_{mode}\eta_{del}}{l_{gain}\tau_2} \int d\lambda \, \frac{Q_P(\lambda)}{n_0 \sigma_2(\lambda)} \left(1 - e^{-(N_1 - \frac{N_3}{2}) n_0 \sigma_2(\lambda) l_{gain}} \right) \left(R_P e^{-(N_1 - \frac{N_3}{2}) n_0 \sigma_2(\lambda) l_{gain}} + 1 \right)$$

$$\tilde{W}_L = \frac{1}{l_{gain}\tau_1} \frac{Q_L}{n_0 \sigma_1} \frac{R_{OC}}{1 - R_{OC}} T_w \left(\frac{1}{T_w^{\,2} \sqrt{R_{OC} R_{HR}}} - 1 \right) \left(1 + \sqrt{\frac{R_{HR}}{R_{OC}}} \right) \tag{3.48}$$

The system of equations is reduced to two coupled integral-transcendental equations for the independent variables N_3 and Q_L which can be solved by standard mathematical packages. In cases where both laser and pump are well described by Gaussian intensity profiles

$$\Theta_P(r) = \exp\left[-2\left(\frac{r}{w_P}\right)^2\right]$$

$$\Theta_L(r) = \exp\left[-2\left(\frac{r}{w_L}\right)^2\right]$$

(3.49)

where w_P and w_L are characteristic dimensions of the pump and laser beams. The modal overlap parameter η_{mode} is calculated from (3.37) to be

$$\eta_{mode} = \frac{w_P^2}{w_L^2 + w_P^2}$$

(3.50)

For beams resembling flat-top profiles such as in the case where diode pump arrays are used and laser cavity is emitting highly multimodal output, the modal overlap parameter is simply

$$\eta_{mode} = 1, \qquad w_P > w_L$$

$$= \frac{w_P^2}{w_L^2}, \quad w_P < w_L$$

(3.51)

We utilize Mathematica's optimum root-finding algorithm in solving this set of equations. Once a valid solution is found, plots of laser performance with respect to many system parameters can be readily generated. In experimental design, the parameters of interest include He buffer gas pressure, operating temperature, output coupler reflectivity, pump power, pump and cavity mode sizes, etc. Once laser

experiment is performed, data can then be critically compared to model predictions and further improvement of model can then be assessed.

A rate equation laser model has been derived from a density matrix formulation. We cannot and do not wish to solve the equations of motion exactly for each atom not only because of the vast amount of computing power required but also because the complexity of solution will obfuscate the basic physics. Through the many layers of simplification, it is abundantly clear that laser physics is at its core a study of approximations. There is a certain satisfaction derived from the ability to start with Schrödinger's equation for a homogeneous ensemble of atoms and arrive at a simple set of rate equations with experimentally meaningful terms involving cross sections, mirror reflectivities and laser output power. However, one must always respect the limitations of the rate equation model and only utilize it when it is fully justified to do so.

Chapter 4 Hydrocarbon-free approach

4.1 Problem of hydrocarbons

Most reported demonstrations to date have used saturated hydrocarbons as the buffer gas or a buffer gas component in the alkali vapor cell. Saturated hydrocarbons such as ethane possess large Rb fine-structure mixing cross sections and have been demonstrated to effectively mix the upper states. This approach, first suggested by Konefal, uses ethane to promote rapid fine-structure mixing, a requirement for efficient laser operation, between the terminal pump level ($^2P_{3/2}$) and the initial laser level ($^2P_{1/2}$).

Although not well reported in the laser publications to date, one issue with this approach is the chemical reaction that takes place between the alkali and the ethane. The chemical reaction, $6X+C_2H_6 \rightarrow 6XH+2C$ (graphite), where X is the alkali (K, Rb, or Cs) and XH is the corresponding hydride, is thermodynamically favored and has a

large negative free energy. In our previous experiments that used ethane as a component of the buffer gas, we observed that carbonaceous deposits formed at cell surfaces (e.g. windows) that simultaneously saw high intensity pump light and were exposed to alkali vapor and ethane gas. Although the deposition of carbon can be a slow process and may not impact experiments over several hours of run time, the problem developed in all of our cells eventually, especially higher temperature cells (T>135° C) as reported by Page *et al* [12]. Examples of the carbon depositing on vapor cell from our previous experiments and at another laboratory are shown in Figure 4.1.
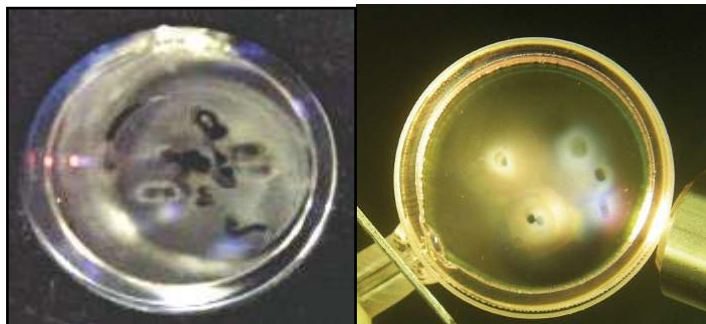
Figure 4.1: Contaminated windows of vapor cell containing alkali vapor and ethane. Photos are taken from laser experiments conducted at LLNL (left) and US Airforce Academy (right)

Because we are ultimately interested in using end-pump geometries in which high intensity pump light is ducted through a cell via reflections with the side walls of the cell where pump light, ethane and alkali vapor meet together, it is essential that we mitigate this problem for reliable power scaling. While the predicted optical to optical efficiencies of >60% have been demonstrated by workers in the field, confirming the anticipated scalability of alkali lasers, the issue of cell degradation has not been resolved.

4.2   The helium solution

Helium, a gas commonly used to broaden the alkali transition lines, has been shown to possess some of the desirable properties of ethane but without the highly undesirable reactions. Based on literature reported data, the Rb-He fine-structure mixing cross section is sufficient to permit efficient diode-pumped Rb based systems at He buffer gas pressures of ~10 atm and higher. Obviated is the issue of carbon formation and degradation of the vapor cell that we observed in our previous alkali laser demonstrations that used ethane as a buffer gas component to promote rapid fine-structure mixing.

4.3   Rubidium laser using pure He gas

A schematic diagram for the experimental setup used to demonstrate the hydrocarbon-free Rb laser is shown in Figure 4.2. The Rb vapor and He gas were contained in a 3 cm long cylindrical ceramic cell with misoriented sapphire windows that were anti-reflection (AR) coated on their external surfaces, but uncoated on their internal surfaces. Rb was introduced into the cell as a pure metal. This was followed by cell evacuation using a laboratory vacuum system and then the introduction of 40 psi of He gas (2.7 atm) at room temperature (~20° C). The entire cell was heated to temperatures up to 170° C, corresponding to a Rb vapor density of 2.2×10^{14} cm^{-3} inside the cell.
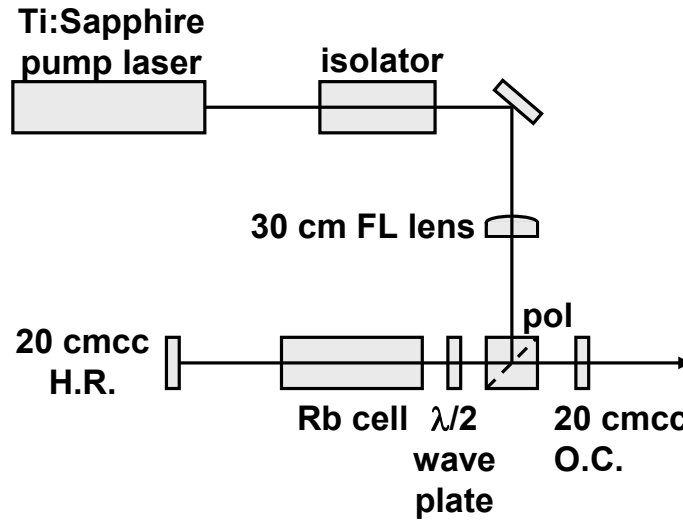
Figure 4.2: Schematic diagram of the experimental setup used in our demonstrations. The laser cavity mirrors have 20 cm radii of curvature and are both concave (cc). H.R. stands for high reflector, O.C. for output coupler and FL for focal length.

The pump source used was a Ti:sapphire laser that produced up to 2.7 W of linearly polarized, near-diffraction-limited CW optical radiation. The Ti:sapphire laser linewidth was ~9 GHz FWHM making the pump laser source narrow compared to the He-broadened D_2 pump absorption feature, which we estimate is ~50 GHz wide based on the known Rb-He collisional broadening rate of 18.1 GHz/amagat. The pump light was coupled into the 40.5 cm long laser cavity via a polarizing beam splitter and traversed the vapor cell twice by reflecting off the highly reflecting end mirror. The end mirror has about 0.99 reflectivity at both the pump and lasing wavelengths. The pump beam was aligned parallel to the laser cavity axis and focused to a 220 μm diameter spot size at the center of the cell, resulting in peak pump irradiances of nearly 5 kW/cm². Since the sapphire windows were soldered onto the cell with optic axes at unknown orientations, a quarter-wave plate was placed in the cavity to partially compensate for the polarization changes caused by birefringence. We estimate that

even with the quarter-wave plate, laser light traversing the cell had a 75% transmission

efficiency passing the cube polarizer on its return path. Coupled with the uncoated

window surfaces, the single-pass passive optical loss is close to 40% in our laser

cavity.
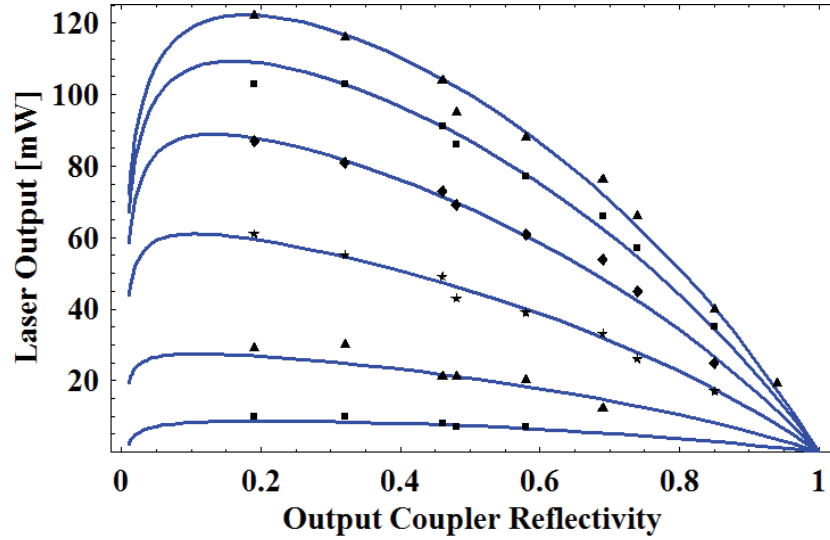
Figure 4.3: Rb laser output power for various pump powers plotted against output coupler reflectivity. Solid curves represent model predictions. From top to bottom, pump powers are: 1.81W, 1.53W, 1.23W, 0.93W, 0.63W, 0.47W.

We successfully observed linearly polarized cw laser emission at 795 nm in a

TEM_{00} beam at cell temperatures in the vicinity of 145° C. Maximum powers of over

130 mW and optical to optical efficiencies close to 7% were measured despite single-

pass passive optical losses near 40% in our laser cavity from cube polarizer and

window reflections. Presented in Figure 4.3 is the theoretical and measured laser

output power versus output coupler reflectivity at several Ti:sapphire pump laser

powers. The reflectivities of the output couplers were directly measured using a

Ti:sapphire probe beam at 795 nm. The reported pump powers were measured outside

the laser cavity and delivered into the laser cavity with an efficiency of 0.9. Large

cavity losses along with the high gains that characterize alkali atoms put the optimal

output coupler reflectivity at below 0.2. These high values for optimized output

coupling support the use of geometrically unstable resonators for the scaling of diode-

pumped alkali lasers to high power with good beam quality. The theoretical curves

overlaying the experimental data points were calculated using the laser model

described in Chapter 3.

Using experimentally measured values and treating the beam overlap and the

Rb-He fine-structure mixing rate as adjustable parameters, we were able to find

excellent agreement between our model and laser output data. The model curves were

generated using an effective Rb-He fine-structure mixing cross section value of

4.6×10^{-17} cm^2 and 51% modal overlap efficiency. Mode overlap is defined in (3.37)

as the fraction of the pump excited volume in the alkali cell extracted by the

circulating laser radiation in the resonator. We attribute the low output power to a

mismatch between the pump and laser beam waists at the cell center and our inability

to get perfect collinear overlap of the pump and the laser beams through the length of

the 3 cm long cell. The pump laser beam waist (1/e-HW) being measured to be 110

μm and the laser mode beam waist estimated to be 75 μm at cell center. We note the

Rb-He fine-structure mixing rate that gave the best fit between our model and

experimental data is approximately three times larger than that predicted based on

cross sections previously reported by Gallagher [22].

Figure 4.4 shows a plot of measured laser output power against cell

temperature, acquired as the cell temperature was continuously varied between 115

and 160°C. For this data the output coupler had a measured reflectivity of 0.19. The

model parameter values used to generate the model overlay of the data in Figure 4.4

are the same as those used for the overlay shown in Figure 4.3.
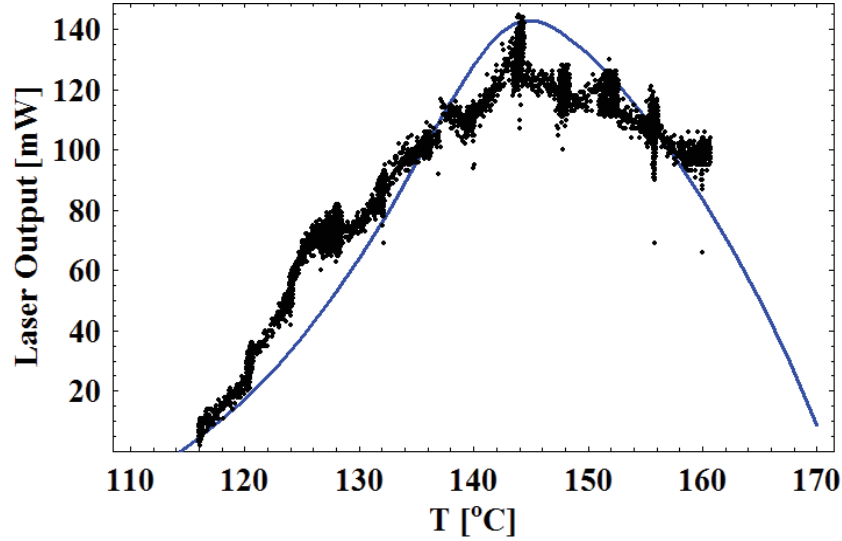
Figure 4.4: Rb laser output power with varying cell temperature using a 0.19 reflectivity output coupler. Solid curve shows model prediction.

Figure 4.5 is a different plot of the data from Figure 4.3 illustrating a feature of

the Rb laser using pure He buffer gas. Both our data and the overlaid laser model

generated curves predict a decrease or roll off in slope efficiency at higher pump

powers. This decrease in slope efficiency is caused by the limited mixing rates

between the Rb fine-structure energy levels. After a Rb atom is optically excited to

$5^2P_{3/2}$ energy level, it radiatively returns to the $5^2S_{1/2}$ ground level or transfers its

energy via He collision to the $5^2P_{1/2}$ initial laser level. Under strong pumping, the

limited fine-structure mixing rate is insufficient in keeping the initial laser level

appropriately filled for optimum laser operation, *i.e.* the initial laser level is essentially

starved for population at the higher pump excitation rates resulting in the observed roll

off in slope efficiency. For this demonstration of the hydrocarbon-free rubidium laser, we purposely picked operating conditions suitable for the Ti:sapphire pump laser that also present a slight bottleneck in laser performance. Agreement between model and experiment supports our understanding of the underlying physical processes. We note here that this saturation behavior is expected to be negligible for power-scaled diode-pumped systems which operate at significantly higher He pressures.
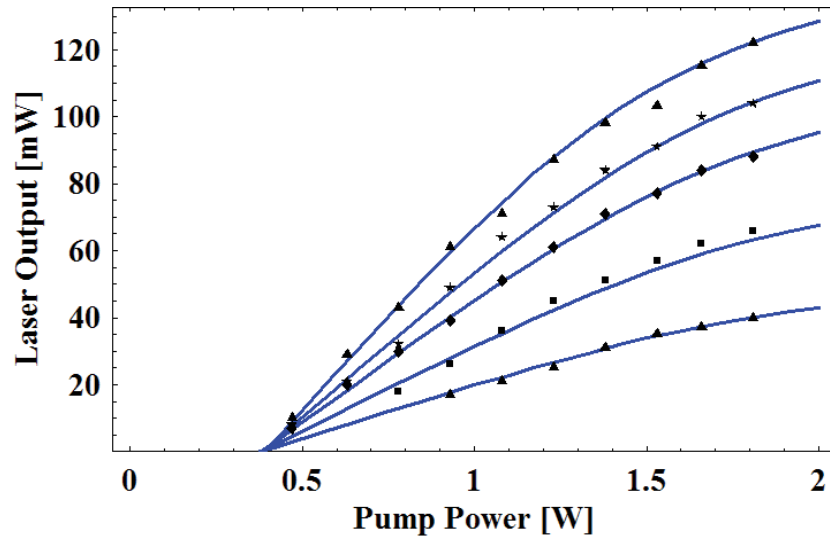
Figure 4.5: Rb laser output power for various output couplers plotted against pump power. Solid curves represent model predictions. From top to bottom, the reflectivities are: 0.19, 0.46, 0.58, 0.74, 0.85. The reflectivities were measured using a Ti:sapphire probe beam at 795 nm.

The same clean, hydrocarbon-free approach being applied here for Rb based systems is also applicable for K-based systems, but not Cs-based systems. This is because the Cs-He fine-structure mixing cross section is too small to make a He-only buffer gas system feasible using Cs. As seen in Figure 2.4, the reported value for the Cs-He fine structure mixing cross section is almost three orders of magnitude smaller than the Rb-He cross section value.

4.4   Advantages of ^{3}He

One potential drawback of the pure He buffer gas approach arises from the smaller fine-structure mixing cross section of Rb-He, known to be orders of magnitude smaller than to that of Rb-ethane. The impact of these differing cross section values means that to achieve equivalent fine-structure mixing rates, higher pressures are required in the pure He systems than would be required in systems using ethane as a buffer gas component. However, higher He pressures lead to larger thermal aberrations under equivalent heat loads. The refractive index variation with temperature dn/dT in the alkali gain cell is proportional to the He pressure, therefore higher He pressures will give larger thermal aberrations under equivalent heat loads. One approach to lowering the required He pressure in the alkali vapor gain cell is replacing the He buffer gas having a natural isotopic abundance with isotopically enriched ^{3}He (natural abundance of ^{3}He:^{4}He is approximately 1:740000).

The advantage of using isotopically enriched ^{3}He stems from its lower mass and therefore higher thermal velocity at a given temperature in comparison with naturally occurring He. The higher thermal velocity associated with ^{3}He increases the fine-structure mixing rate, $\gamma_{^2P_{3/2}\rightarrow^2P_{1/2}} = n_{He}\sigma_{^2P_{3/2}\rightarrow^2P_{1/2}}v_r$, where n_{He} is the number of He atoms per unit volume, $\sigma_{^2P_{3/2}\rightarrow^2P_{1/2}}$ is the Rb-He fine-structure mixing cross section, and v_r is the mean relative speed between He and Rb atoms.   First, at a given temperature v_r is higher in ^{3}He than ^{4}He by $\sqrt{4/3} \approx 1.15$, which not only benefits the fine-structure mixing rate which depends directly on v_r, but also improves thermal management in

the cell. Since the thermal conductivity κ of a gas to lowest order is proportional to the mean particle velocity, κ of ^{3}He is larger than that of ^{4}He by the same factor. Secondly, the fine-structure mixing cross section itself has a velocity dependence that is expected to give a Rb-^{3}He value larger than the Rb-^{4}He value at a given cell temperature due to the difference in thermal speeds of the two He isotopes [22]. It can be extrapolated from that velocity dependence that the Rb fine-structure mixing cross section in ^{3}He is approximately 1.5 times larger than that of ^{4}He at our operating temperatures. Together, one can expect a Rb fine-structure mixing rate about 1.7 times larger for the ^{3}He system than the ^{4}He system under same operating conditions. A summary of significant system parameters is provided in Table 4.

Table 4: Important physical parameters for Rb laser performance and a comparison between systems using ^{3}He and ^{4}He. n_{He} is the number density of He atoms. λ_{MFP} is the mean free path.

Physical Parameter	Expression	$\dfrac{\text{Value for} ^3\text{He}}{\text{Value for} ^4\text{He}}$
Mean particle velocity	$v_r = \sqrt{\dfrac{8}{\pi}\dfrac{k_B T}{\mu}} \approx \sqrt{\dfrac{8}{\pi}\dfrac{k_B T}{m_{He}}}$	$\sqrt{4/3} \approx 1.15$
Rb-He fine-structure mixing cross section	$\sigma_{^2P_{3/2}\to^2P_{1/2}}$ (Experimentally determined [22])	1.5 at 142°C
Fine-structure mixing rate	$\gamma_{^2P_{3/2}\to^2P_{1/2}} = n_{He}\sigma_{^2P_{3/2}\to^2P_{1/2}} v_r$	1.7
Thermal conductivity	$\kappa = n_{He} v_r \lambda_{MFP} k_B$	$\sqrt{4/3}$
Collisional broadening rate of Rb D$_2$ line	(Experimentally determined [27])	1.15

In view of these advantages of ^{3}He over ^{4}He based systems, we expect the ^{3}He approach to be the preferred route to power scaling DPAL lasers to efficient, reliable, and good beam quality systems.

4.5   *Rubidium laser using ^{3}He gas*

The experimental setup used in this demonstration is nearly identical to that used in Section 4.3 which had used naturally-occurring He as the buffer gas is shown in Figure 4.6. The chief difference is the type and placement of the waveplate. The Rb vapor and ^{3}He gas were contained in a similar 3 cm long cylindrical ceramic cell with sapphire windows that were anti-reflection (AR) coated on their external surfaces, but uncoated on their internal surfaces. The cell was evacuated using a laboratory vacuum system followed by the introduction of 40 psi of ^{3}He gas (2.7 atm) at room temperature (~20°C). The ^{3}He gas is manufactured by Spectra Gases Inc. with a quoted 99.999% chemical purity and 99.9% isotopic enrichment.
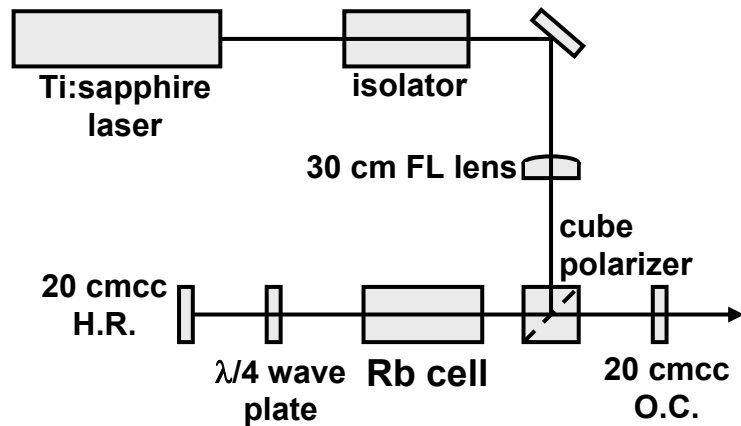
Figure 4.6. Schematic diagram of the experimental setup used in our demonstrations. The laser cavity mirrors have 20 cm radii of curvature and are both concave (cc). H.R. stands for high reflector, O.C. for output coupler and FL for focal length. The Rb cell is enclosed in a heated copper oven.

The pump source used was a Ti:sapphire laser that produced up to 2.4 W of linearly polarized, near-diffraction-limited cw optical radiation. The Ti:sapphire laser linewidth was ~9 GHz FWHM making the pump laser source narrow compared to the He-broadened D_2 pump absorption feature, which we estimate is ~50 GHz wide based on the known Rb-^{3}He collisional broadening rate of 20.8 GHz/amagat. The pump light was coupled into the 41.5 cm physical length laser cavity via a polarizing beam splitter and traversed the vapor cell twice by reflecting off the highly reflecting end mirror. Using the same experimental setup, the pump beam was aligned parallel to the laser cavity axis and focused to a 220 μm diameter spot size at the center of the cell, resulting in peak pump irradiance of nearly 5 kW/cm^2. A stable cavity mode is formed with aid from gain guiding due to the nonuniform transverse gain profile over the length of the cell. A quarter-wave plate was placed in the cavity to partially compensate for the same polarization problem caused by birefringence of the sapphire windows. We estimate that even with the quarter-wave plate, laser light traversing the cell had a 75% transmission efficiency passing the cube polarizer on its return path. Coupled with the uncoated window surfaces, the single-pass passive optical loss is close to 40% in our laser cavity.

Laser emission at 795 nm in a TEM$_{00}$ beam was observed at cell temperatures in the vicinity of 150°C. Maximum output powers of over 350 mW were measured, corresponding to an optical-optical conversion efficiency greater than 21%. Large cavity losses along with the high gains that characterize alkali atoms place the optimal output coupler reflectivity below 0.2. Presented in Figure 4.6 is the theoretical and

measured laser output power versus pump power using different output couplers at a cell temperature of 142°C. The theoretical curves overlaying the experimental data points were calculated using our laser model. Because of the larger Rb-^{3}He inelastic collision cross section compared to that of ^{4}He, the mixing rate between the fine-structure levels is high enough to maintain efficient lasing at these pump levels. The saturation effect observed in our previous demonstration for the Rb-^{4}He laser in which the slope efficiency decreased at higher pump powers due to insufficient fine-structure mixing is significantly diminished here with nearly identical operating conditions, supporting the use of ^{3}He with its larger fine-structure mixing rate for power scaled systems. Based on measured pump beam characteristics and the cavity dimensions, we treated the Rb-^{3}He fine-structure mixing rate and the mode overlap efficiency as adjustable parameters over a reasonable range. The model curves were generated using an effective Rb-^{3}He fine-structure mixing cross section value of 7.1×10^{-17} cm^2 and 57% mode overlap efficiency. We note the Rb-^{3}He fine-structure mixing rate that gives the best fit between our model and experimental data is, as expected, approximately 1.5 times larger than our model-fitted value for the Rb-^{4}He cross section.
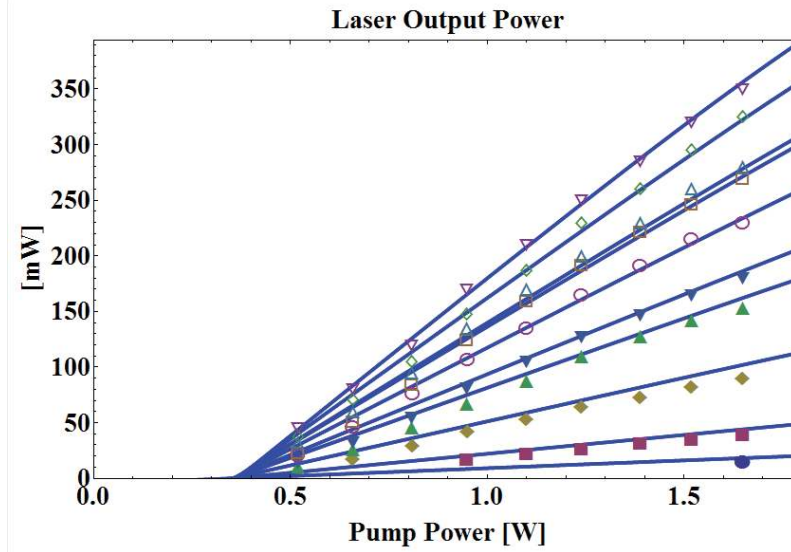
Figure 4.6: Rb laser using ³He output power for various output couplers plotted against pump power. Solid curves represent model predictions. From top to bottom, the reflectivities are: 0.19, 0.32, 0.46, 0.48, 0.58, 0.69, 0.74, 0.85, 0.94 and 0.976. The reflectivities were measured using a Ti:sapphire probe beam at 795 nm.

We have demonstrated the operation of a 795-nm Rubidium resonance laser system using a buffer gas consisting of pure ^{3}He. The use of pure He for the buffer gas, either natural abundance or isotopically enriched ^{3}He, as opposed to the more common approach to date of using a hydrocarbon containing buffer gas should enable high reliability Rb based diode-pumped alkali laser (DPAL) systems by eliminating the carbon deposition problem in the laser cells that occurs with the hydrocarbon approach. For our pure He buffer gas approach, the use of isotopically enriched ^{3}He offers multiple advantages over the use of naturally occurring He. The higher thermal velocity of ^{3}He over that of ^{4}He give a Rb fine-structure mixing rate about 1.7 times larger for the ^{3}He system than the ^{4}He system under the same operating conditions. The higher fine-structure mixing rate, which is critical for efficient laser performance, enables comparable performing ^{3}He systems at only ~60% of the He buffer gas

pressure required for the ^{4}He systems. Since thermal aberrations in the laser's Rb vapor cell are governed by dn/dT which is proportional to the He pressure, the ^{3}He approach will be advantageous for high beam quality lasers in power scaled system.

Due to their projected efficiency advantages over diode-pumped solid state lasers, their compatibility with commercially available laser diode arrays, and now a demonstrated system that promise very high reliability, diode-pumped ^{3}He-only Rb lasers will potentially compete favorably with DPSSL's in many applications that require high beam quality cw or quasi-cw laser operation.

This chapter contains material that has been submitted for publication as it may appear in S. S. Q. Wu, T. F. Soules, R. H. Page, S. C. Mitchell, V. Keith Kanz, R. J. Beach, Opt. Lett. 32, 2423-2425 (2007) and Optics Communications, Vol 281, 5, 1222-1225 (2008). The dissertation author was the primary investigator and author of this paper.

Chapter 5　　Diode-pumped alkali laser (DPAL)

5.1　　Diode pumping for higher average power

Experiments described thus far demonstrate the high potential of the hydrocarbon-free rubidium laser. However, the output power of alkali lasers pumped by Ti:sapphire lasers does not usually exceed the watt level because of the limited power of the excitation source. The total wall plug efficiency of such devices is also very low because of the low efficiency of the pump laser. From the very beginning of alkali laser research and development, a focus of attention was the possibility of using efficient and high power diode laser arrays as excitation sources for alkali lasers. The main obstacle limiting usage of high power diode lasers for alkali pumping is due to their poor spatial and spectral properties. In this chapter, we present results from our diode-pumped experiments illustrating our methodology and achievements in this field.

5.2 *Laser design*

5.2.1 Optical pump source

To deliver the optical excitation power required, multiple packages of diode

arrays were optically combined into a single pump spot by use of the optical apparatus

shown in Figure 5.1.
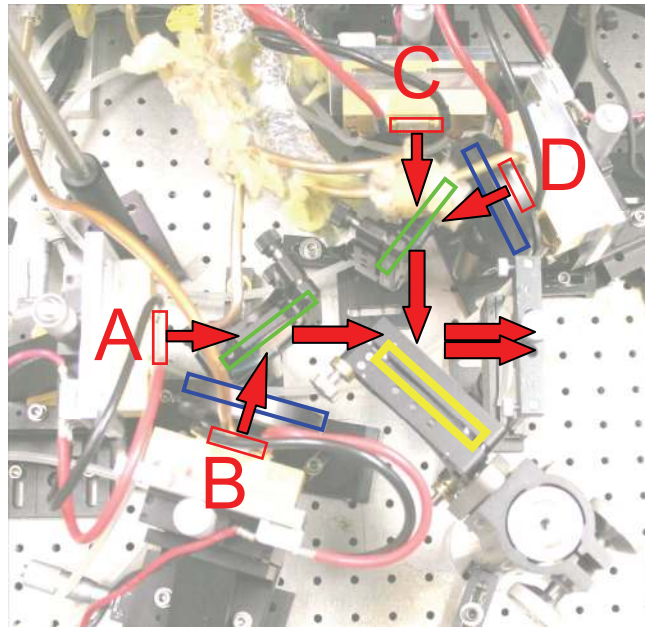
Figure 5.1: Diagram of diode laser array setup. The red boxes represent the diode laser arrays (A-D) and the red arrows represent their output. The green boxes denote the location of the thin-film polarizers. The blue boxes denote the location of the half-wave plates. The yellow box represents a silver coated mirror.

Outputs from four separate diode laser arrays A through D are combined

together using a polarization and spatial combination techniques. Outputs from array

B passes through a half-wave plate and therefore has its polarization rotated by 90°

with respect to the output from array A. The thin-film polarizer is set at an angle for

maximum transmission of array A which also maximizes the reflected light coming

from array B. After traversing this thin-film polarizer, the two beams are collinear and have similar spatial characteristics. Outputs from diode arrays C and D are treated in the same manner but travelling at 90° from the first pair. The mirror is placed such that it passes the beam travelling horizontally in the diagram and reflects the beam travelling vertically. The mirror is carefully adjusted so that the outputs of the two beams are spatially adjacent to each other with minimal gap in between.

For the output from each of the four diode arrays to travel collinearly after combination requires near-perfect alignment. Since the radiation from the diodes has relatively low spatial quality, this can only be achieved with limited accuracy. A realistic estimate of the pointing accuracy we can achieve in this fashion is no smaller than about 3° = 50 mrad. However finer adjustments can be made at the beam focus after the optical delivery system where small angular deviations translate to measurable shifts in position. After this alignment process is done, we estimate the effective divergence in the combined beam to be ~25 mrad.

5.2.2   Optical delivery system

After the pump light from the diode laser arrays is combined together, it still needs to be formatted and delivered to the vapor cell. The optical apparatus used to transfer the pump light to its destination in the laser cavity is shown in Figure 5.2.
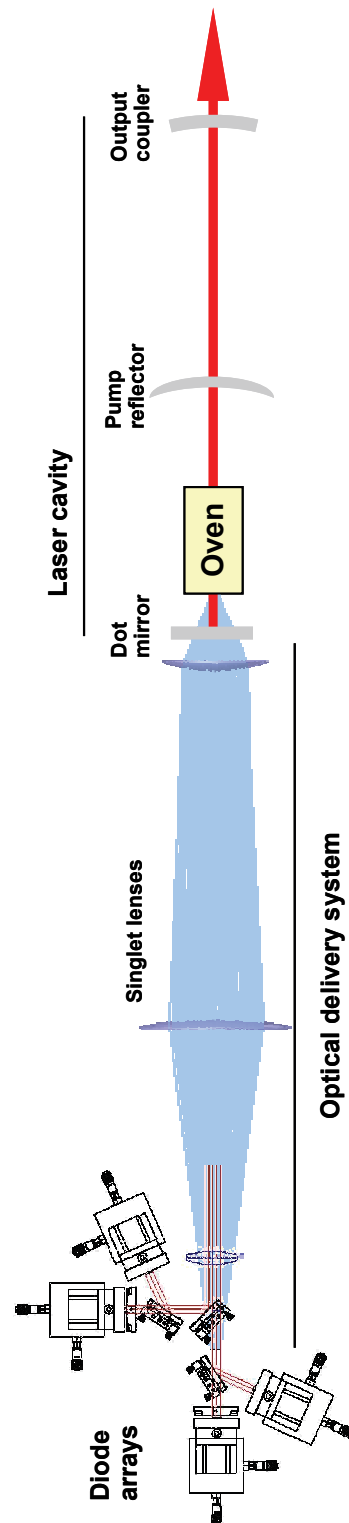
Figure 5.2: Diagram of optical delivery system and laser cavity. The optical delivery system takes the combined beams from the diode arrays and delivers it into the vapor cell (held inside the oven). It comprises of a negative cylindrical lens followed by two positive spherical lenses.

The light coming out of the diode arrays is not in the optimal beam format for our purpose. We wish to focus the pump beam as tightly as possible for the highest pump intensity but with the smallest divergence as possible so that we make the minimum amount of bounces in the cell. The long spatial dimension (fast axis) of the beam is also the dimension that is near-collimated. Hence in this dimension the beam can be tightly focused at a cost of increased beam divergence. In the other dimension (slow axis), the angular divergence is greater than 150 mrad, so we can only moderately shrink the spatial dimension before reaching the limit on tolerable angular divergence.

A three-lens system comprising of two spherical singlet lenses and one negative cylindrical lens does what is prescribed. In the slow axis of the diode lasers, only the spherical lenses have optical power. The focal lengths of the first and second spherical lenses are 33 and 10 cm, respectively. By spacing the lenses apart by their total focal length of 43 cm, the lens pair forms a simple telescopic imaging system which produces an image of the front focal plane at the back focal plane with a 3.3x demagnification. The size of the image at the entrance of the cell in this dimension is then approximately 1/3.3 cm = 3 mm.

In the fast axis which is also the near-collimated direction, the cylindrical lens with a focal length of -15 cm provides additional image reduction. The negative cylindrical lens is placed approximately one focal length from the diode laser sources. By classical imaging analysis, a plane wave traveling at an angle of θ with respect to the optic axis is transformed by a lens to a point at the focus a distance $f\theta$ away from

the axis. Hence a near-collimated source with a maximum beam divergence of 25 mrad appears to have an effective spatial dimension of $15 \times 0.025 = 0.3$cm. After transmitting through the 3.3x image reduction telescope, the estimated focal spot is ~1.1 cm.

The measured beam spot at the focus (imaging plane) of the lens system and spectral characteristics are depicted in Figure 5.3. The measured beam parameters then determine the size of the light duct in the cell. Based on beam profile data, we estimate that about half of the light is concentrated inside the central 3.2×1.3 mm rectangular region of the beam.
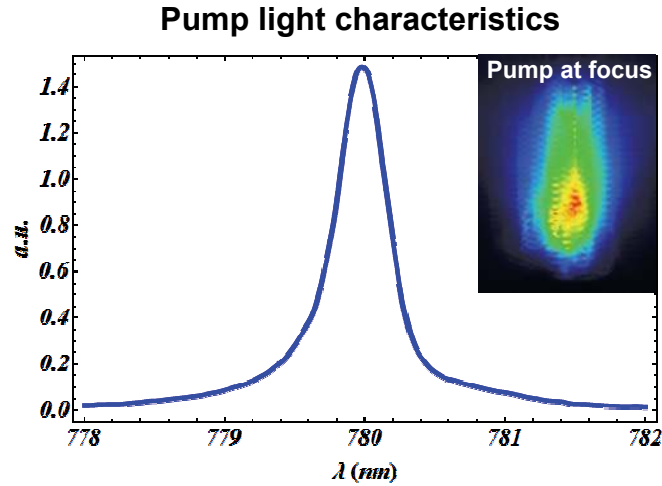
Figure 5.3: Spectral and spatial characteristics of the diode pump beam measured after delivery optics.

5.2.3   Cell geometry

The vapor cell with a total length of 9 cm is made from industry-standard stainless-steel vacuum parts. Figure 5.4 shows how the cell is formed. A vacuum

valve seals the interior of the cell from the external atmosphere when the cell is complete.
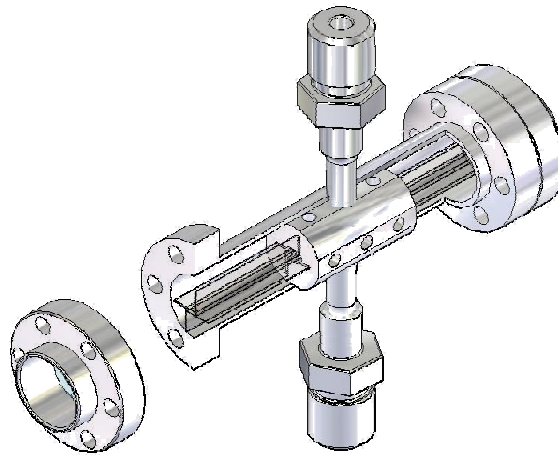
Figure 5.4: Diagram of vapor cell showing the internal structure.

Inside the cell, there is a delicate light duct made out of the sapphire pieces and a holding structure. The light duct is formed by 4 sapphire pieces placed in orthogonal directions as shown in Figure 5.5. The pump light enters through the opening on one end and travels down the duct via reflections off the internal surfaces of the sapphire pieces.
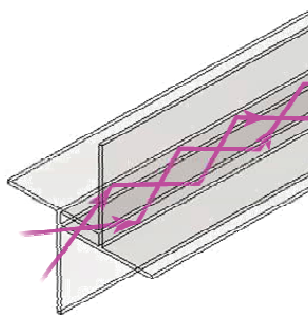
Figure 5.5: Four sapphire pieces form a light duct for pump light.

The sapphire pieces were coated by Deposition Sciences, Inc. (DSI) with a highly reflective 36 layer coating structure made from zirconia (ZrO_2) and alumina (Al_2O_3), where the final layer is alumina. The optical coating is designed to reflect 780 nm light at high angles of incidence. The light duct is held in place by a stainless-steel holder with vacancies fitted for the four sapphire pieces. The sapphire pieces form a duct with an interior dimension of 3.2×1.3 mm. To gauge the transport efficiency of the light duct formed by the sapphire pieces, a power measurement was taken using a rectangular aperture with the same dimensions as the opening of the light duct. It is found that about half of the power delivered to the cell makes it inside the aperture of the light duct, and two-third of that light entering the duct exits the cell from the other end of the light duct. The amount of light that does not exit the cell is simply absorbed by the cell walls or the holding structure.

5.2.4   Thermal considerations

The pump power delivered to the cell is measured to be 1.2 kW. Even if a fraction of the incoming pump light is absorbed by the cell, either on the walls or in the internal holding structure, the resulting rate of temperature rise can be quite significant. We experimentally tested the temperature rise in our cell under continuous pumping and found temperature rises exceeding 50° C in less than 10 seconds. Since this value was measured at the exterior surface of the cell, we anticipated that the temperature rise inside the cell is likely much higher. With such a significant thermal deposition in the cell, the Rb vapor density is expected to vary far from initial values. Furthermore, if heat dissipation is nonuniform, one can expect

thermodynamic gradients to form and thus cause more uncontrolled thermal variations inside the cell.

Because of these and other issues, we first refrained from applying cw pump excitation and instead used controlled pulses of pump light. The diode current drivers were set to create 100 μs pulses at 10 Hz, or a duty cycle of 0.1%. At this periodicity, the residual thermal effects are minimal.

5.2.5 Laser model

The same laser model used for our Ti:sapphire experiments can be extended to the diode-pumped case. However in the diode-pumped experiment, it is necessary to include the optical losses attributed to the light duct in our model. A modified expression of the excitation rate is derived including the transport losses of the light duct. The quasi-steady state solution of the propagation equation of the pump field through the light duct is

$$\frac{dI_P}{dz} = -(n_1 - \tfrac{1}{2}n_3)\sigma_2 I_P - \alpha I_P, \qquad (5.1)$$

where α represents a distributive loss coefficient along the direction of propagation. Substituting (5.1) into (3.36), we find that

$$W_P^{(lossy)} = W_P - \frac{\eta_{del}}{V}\int d\lambda \int_{\text{laser mode}} d^3r \frac{\alpha I_P}{hc/\lambda} \qquad (5.2)$$

An estimate for the second term can be found by using an approximate solution for the pump field in the presence of transport losses: $I_P^{+}(z) = I(0)\exp[-(n_1 - \tfrac{1}{2}n_3)\sigma_2 z - \alpha z]$. This would be an "exact" solution if the population density of each state is uniform

along the cell which is typically not true in longitudinally pumped lasers. Nevertheless it is a fair approximation as a first estimate. After simplification, the total excitation rate in normalized variables can be expressed as,

$$\tilde{W}_P^{(lossy)} = \frac{\eta_{mode}\eta_{del}}{l_{gain}\tau_2} \int d\lambda \frac{Q_P(\lambda)}{n_0\sigma_2(\lambda)} \left(1 - e^{-[\alpha+\kappa(\lambda)]l_{gain}}\right) \left(R_P e^{-[\alpha+\kappa(\lambda)]l_{gain}} + 1\right) \left(1 - \frac{\alpha}{\alpha+\kappa(\lambda)}\right)$$

(5.3)

where $\kappa(\lambda) = (N_1 - \frac{N_3}{2})n_0\sigma_2(\lambda)$.

5.3   Experimental results

The cell was filled with 11 atm of naturally-occurring He at room temperature before being wrapping in insulating material and fitted with electric heaters. Laser emission at 795 nm was observed at cell temperatures in the vicinity of 160°C. Presented in Figure 5.6 is the measured laser output power versus output coupler reflectivity at several delivered pump powers. Maximum powers of over 150 W were measured in a multimodal beam emitted from the laser cavity. The reported pump powers were measured through an approximate aperture at the minimum beam spot at the entrance of the cell. The peak optical to optical conversion efficiency obtained was 26%, in general agreement with model predictions. The output beam exhibited almost rectangular shape coinciding with the light duct aperture suggesting good modal fill of the laser mode in the cell. In this experiment, there was no effort made in applying laser mode control. Hence the cavity supported a large number of high order modes due to the relatively large excited gain region. In power-scaled systems, the

large absorption cross sections that characterize the alkalis give high unsaturated gains that are well-matched to unstable resonator requirements. Unstable resonators provide a means in extracting the high output powers while maintaining near diffraction-limited beam quality.

Diode-pumped Rb laser in 100µs q-cw operation
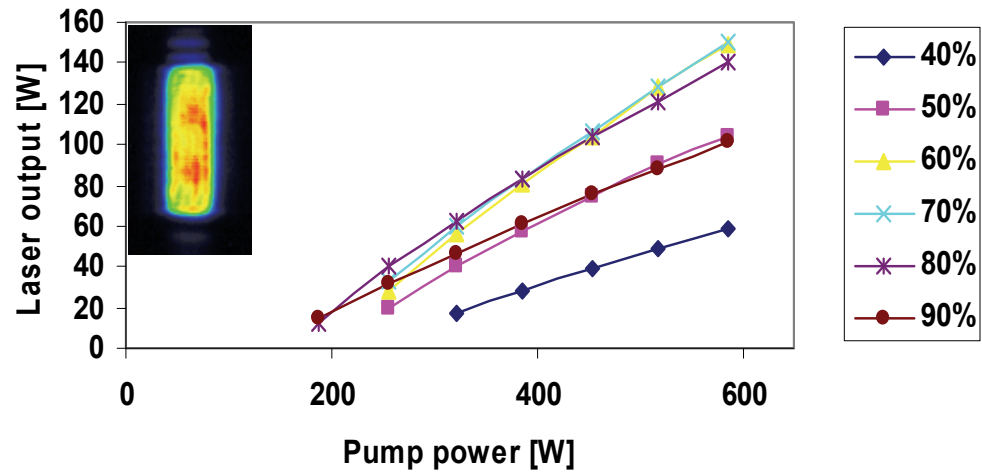
Figure 5.6: **Rb laser output power for various output couplers plotted against pump power delivered into to the cell. The inset shows a beam profile of the laser output. The diode arrays were set to emit in 100 µs pulses due in part to thermal considerations.**

5.4   *Discussion*

Using experimentally measured diode array pump spectra and values for various laser parameters, we are able to find agreement between our model and laser output data. Due to the sufficiently high density of He already in the cell used in the broadening of the transition lines, no sign of laser bottlenecking is observed. [3]He provides more rapid fine-structure mixing, however it is not necessary in this experiment. Agreement with model supports further pursuit of this approach.

When continuous pump excitation was applied to the vapor cell, we were unable to obtain stable laser output over seconds of run time. In many cases, the cell temperature rose significantly along with the Rb vapor density due to the deposition of pump power in the cell. Figure 5.7 shows one such experimental run where the laser output quickly decayed over 100 ms of run time. In other trial runs, we were able to obtain up to few seconds of laser output, but in all cases, there were dramatic decays or disappearances of laser output.
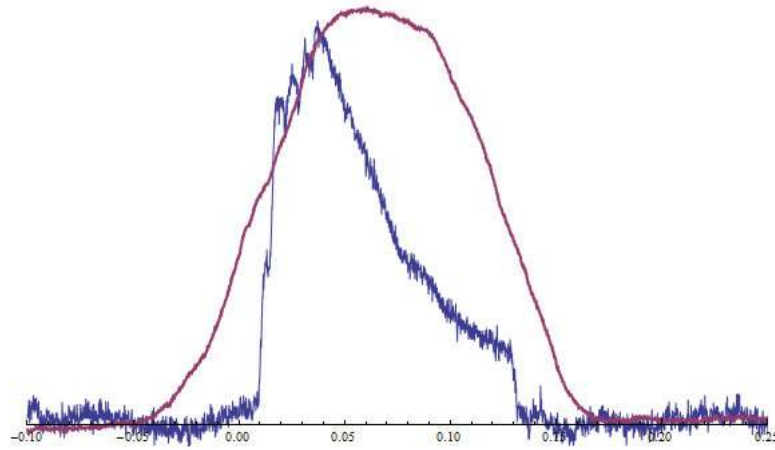
Figure 5.7: Normalized plots of the laser output (blue) and transmitted pump light (purple) in one trial run where the cell was pumped continuously for ~130 ms. The decay of the laser output is due to thermally induced variation of the rubidium vapor pressure.

Our hypothesis that the Rb vapor density is rapidly increased is confirmed when we compare the transmitted pump light with a cell devoid of Rb. Figure 5.8 clearly shows a sharp increase in pump absorption indicating that the Rb vapor density has significantly increased due to the rapid rise in cell temperature. The vapor is likely evaporated from the sapphire light duct or the nearby cell walls.
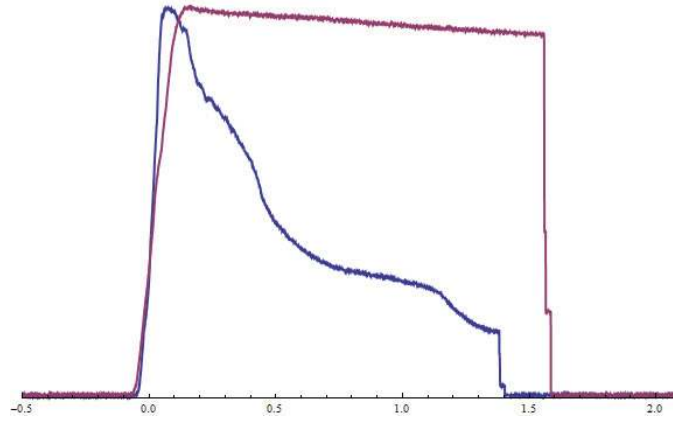
Figure 5.8: Measured pump power transmitted through a vapor cell with Rb (blue) and without Rb (purple). The sudden decrease of transmitted light in the cell with Rb is a result of rapid increase in Rb vapor density caused by heat. The traces were taken in two separate runs with slightly different pulse lengths close to 1.5 seconds.

In power-scaled alkali laser systems pumped by 100's kW to MW of diode radiation, the tremendous thermal deposition will require the use of flowing gas systems. The flow of gas removes heat from the pumped region to maintain near-diffraction-limited beam quality, and at the same time, helps maintain a constant Rb vapor density inside the cell. We do not anticipate that this thermally-induced phenomenon will persist in power-scaled system with flowing gas.

To the best of our knowledge, this is the first time that a 100 W-class quasi-cw alkali laser has been demonstrated with $\geq$0.5nm bandwidth laser diode pump source. Based on our results, the hydrocarbon-free DPAL present a new pathway to high average power lasers with good beam quality and high efficiency.

Chapter 6   Ionization-induced phenomena

6.1   Introduction

While we have thus far treated the laser processes in a simple three-level

system and have achieved good agreement with measured results, this is ultimately an

incomplete picture. Little attention has been paid to kinetic processes outside of the

intramultiplet mixing between the lowest excited p states required for lasing.

Typically in atomic species, there is a vast set of energy configurations accessible to

the active atoms. To better understand the behavior of the Rb laser, one must take

kinetic processes between these other energy levels into consideration.

As in the case of typical atomic systems, there is a vast set of energy

configurations accessible in the electronic structure. The alkalis have a hydrogen-like

electronic structure as discussed in Chapter 2. Alkalis and especially Rb and Cs are

two of the most easily ionized atomic species with ionization potentials of about 4 eV.

Their single outer s-electron tends to be loosely bound and can be freed by
photoionization or collisional ionization processes.

Many investigations of laser-induced ionization phenomena have been
previously conducted by workers in the field; for example see [36,37,38,39]. Based
on published findings, some of these phenomena are also present in alkali lasers and
should manifest themselves in the laser output. Using a chopped Ti:sapphire laser as
an excitation source, we systematically observed some of these processes and
developed a simplified model that reproduces their main features. Drawing on the
previous works that have investigated various processes that are parasitic to our laser
kinetics, we apply those results to the Rb-He system. Finally we analyze whether
these processes pose any performance limitations for the Rb laser. We will attempt to
exploit some of their previous work and apply their results to the Rb-He system.
However since many of the previous work have been conducted in a pure alkali vapor
environment or with a low density buffer gas (<<1atm), care must be taken to justify
the validity of using their measured results in our system which has a much higher
density of buffer gas atoms. We will analyze the details of each of these processes and
determine their resulting transition rates. We will then analyze the limits if any these
processes pose to the Rb laser.

6.2   Experimental observations

A schematic diagram for the setup used in our experiments is shown in Figure
5.1. The pump source used was a Ti:sapphire laser that delivered up to 1.6 W of
linearly polarized, near-diffraction-limited cw optical radiation at 780 nm to the vapor

cell which contained Rb vapor and naturally occurring He gas. The pump beam was aligned parallel to the laser cavity axis and initially focused to a 250 μm diameter spot size at the center of the cell, resulting in a peak pump irradiances of nearly 7 kW/cm^2. We later reduced the beam diameter to 170 μm effectively doubling the peak intensity. A mechanical chopper wheel with a duty cycle of 1/30 was placed in the pump beam before the introduction to the laser cavity to control the duration and frequency of the transmitted pump pulse.
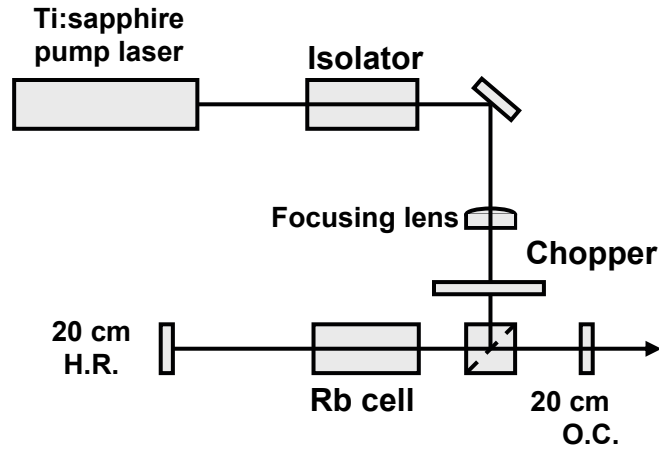
Figure 6.1: Schematic diagram of the experimental setup used in our demonstrations. The laser cavity mirrors have ~20 cm radii of curvature and are both concave (cc). H.R. stands for high reflector, O.C. for output coupler.

A Ti:sapphire laser is preferred as the pump source for this experiment because its narrow linewidth and small diffraction-limited beam size, which along with pulse duration control, help eliminate effects due to broad spectrum excitation, thermal deposition, hydrodynamic processes and wall interactions. The time scales over which these processes occur are longer than the millisecond of runtime in our experiment and can be neglected in the analysis. Generally, these processes may need to be considered in analysis involving continuous wave operation.

Laser emission at 795 nm in a TEM_{00} beam was observed at cell temperatures in the range of 115 -155°C, He fill pressures of 4 atm and 11 atm, and pump irradiances of ~7 kW/cm^2 and ~14 kW/cm^2. The emitted laser output is recorded and shown in Figure 6.2 along with calculated curves produced using our laser model. The model traces are created using ionization and recombination rates based on literature reported experimental results. Over a 1 ms pump pulse, time-varying behavior in the laser is clearly evident, provoking our interest in further study. Note that relaxation oscillations due to cavity-media interaction generally occur on a sub-microsecond time scale for this laser. Hence relaxation oscillation is not a reasonable explanation for our experiment observations. We will show that multilevel energy transfer processes can explain the bulk of the observed laser output behavior.
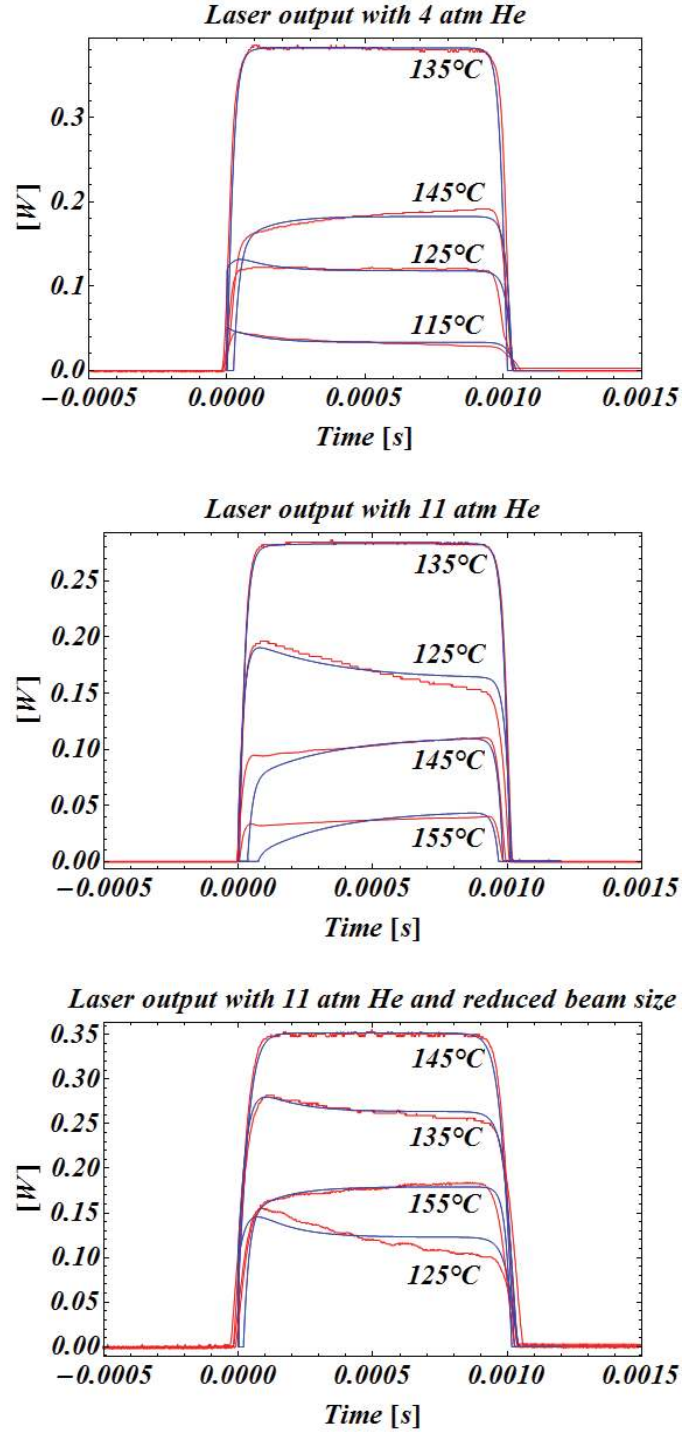
Figure 6.2: **Measured traces (red) and model generated curves (blue) of Rb vapor laser output with (a) 4 atm He (measured at ~20°C), 30% output coupler reflectivity and pumped by 250 μm diameter beam; (b) 11 atm He (measured at ~20°C), 40% output coupler reflectivity and pumped by 250 μm diameter beam; (c) 11 atm He (measured at ~20°C), 40% output coupler reflectivity and pumped by 170 μm diameter beam.**

6.3   *Physical processes*

6.3.1   Energy pooling

Here we briefly review the dominant processes considered in our model. Energy pooling occurs during collisions of two excited atoms. In the collision, the energy of one of the colliding partners is transferred to the other. One loses its energy and drops back to the ground state; the other takes up the lost energy and jumps to the nearest available energy state. Symbolically, energy pooling corresponds to the reaction

$$M^* + M^* \rightarrow M^{**} + M + \Delta E \qquad (6.1)$$

where M* is an optically-excited alkali atom in the lowest lying p states and M** is an excited atom in a higher energy state and ΔE is the energy defect of the reaction. The rate at which this process occurs tends to vary inversely with the energy defect. The most resonant energy pooling reaction in the alkalis occurs in Rb. The Rb 5d state has nearly twice of the energy of the $5^2P_{3/2}$ state, $\Delta E = -68$ cm^{-1}, which is well within thermal energy kT at room temperature. This process contributes to the 421 nm light often seen from excited Rb vapor as result of the final step in the 5d→6p→5s cascaded transition. An experimental study of the energy pooling process, $Rb(5^2P_{3/2}) + Rb(5^2P_{3/2}) \rightarrow Rb(5d) + Rb(5s)$ was carried out in [40] with a reported cross section of $(3 \pm 1.5) \times 10^{-14}$ cm^2 at 450 K. The same process was also studied in [41] with a cross section of $(2.50 \pm 1.12) \times 10^{-14}$ cm^2 at 330 K.

6.3.2   Photoexcitation

This near coincidence of the Rb 5d energy and $5^2P_{3/2}$ energy levels also allows Rb atoms to be optically excited into the 5d level from $5^2P_{3/2}$ as a result of the spectral wing of the 776 nm absorption feature. The oscillator strength of the $5^2P_{3/2} \rightarrow 5^2D_{5/2}$ transition is $f_a = 0.0366$ and the $5^2P_{3/2} \rightarrow 5^2D_{3/2}$ transition is $f_b = 0.00432$ [42]. Both transitions contribute because of their relative proximity to each other. Assuming ideal homogeneous lineshapes with similar broadening coefficients for each transition, an estimate of the total $5^2P_{3/2} \rightarrow 5d$ absorption cross section can be obtained from the expression $\int \sigma_{5P_{3/2} \rightarrow 5D} \, dv = (f_a + f_b)\pi r_e c$, where r_e is the classical electron radius and c the speed of light.

Similarly, the same analysis can be given for broadband sources. Because of the broader spectrum, a significant portion of the energy resides in a spectral region less than 4nm away from 776nm. The resulting transition rate is correspondingly larger. Generally, the broader the pump source spectrum, the larger this transition rate becomes. Diode array pump sources with linewidths of ~0.5 nm are common in diode-pumped experiments. It is important to note that while most of the radiation may reside in this 0.5 nm region, nevertheless a significant fraction of the diode light resides in a wider pedestal under the main spectral lobe with a width up to several nanometers.

6.3.3 Penning ionization

Once highly excited atoms are produced, a second collision with an excited atom can result in ionization. Penning ionization consists of collisions between two excited atoms where one atom loses its energy and goes back to the ground state, while the other atom by taking up the additional energy of the first atom now has enough energy to overcome the ionization potential, resulting in an ion and a free electron. Symbolically, this corresponds to

$$M^* + M^{**} \rightarrow M + M^+ + e^- \tag{6.2}$$

where M** represents a highly excited alkali atom within one excitation energy of the ionization potential and M$^+$ is a singly-ionized alkali atom. The Penning ionization process, $Rb(5p) + Rb(5d) \rightarrow Rb(5s) + Rb^+ + e^-$, was measured in [43] with a reported rate of 3.5×10^{-8} cm^3/s at 470 K.

6.3.4 Photoionization

Concurrently, many of the highly excited states are within one excitation step of the ionization potential and thus an atom in one of these states may be photoionized by absorption of a single pump or laser photon. The peak cross section at the operating wavelength is 16×10^{-18} cm^2 from the 5d level [44]. Based on this value, we find that the photoionization rate is still smaller than the Penning ionization rate at our peak pump intensity of 14 kW/cm^2.

6.3.5 Recombination processes

Recombination of ionized Rb atoms and molecules occurs by a variety of processes. Atomic ions may undergo radiative and three-body recombination. Three-body recombination is typically faster than direct radiative recombination. The third-body participates in the process by removing the excess energy from the ion-electron pair allowing it to recombine into a neutral atom,

$$M^+ + e^- + A \rightarrow M + A \qquad (6.3)$$

where A represents either another alkali atom, a free electron, or a buffer gas atom. The total radiative recombination coefficient in Rb is $\beta_{radiative} = 2.24 \times 10^{-12} cm^3 / s$ [45]. This corresponds to a comparatively long characteristic timescale on the order of seconds under our experimental conditions. Hence recombination of Rb ions and electrons is dominated by a three-body process where the third body may be a free electron, Rb atom, or He atom. The process of recombination with participation of neutral atom is discussed in [46,47]. In Gaussian units, the rate coefficient is calculated to be

$$\beta_{Rb-e-He} = \frac{16}{3}\sqrt{2\pi}\,\frac{2m_e}{M_{He}}\,\frac{e^6\sigma_t}{m_e^{\frac{1}{2}}(kT)^{\frac{5}{2}}}, \qquad (6.4)$$

where σ_t is the transport cross-section for electron scattering by a He atom. Using kT = 0.04 eV, $n_{He} = 10^{20}$ cm^{-3} and a cross section based on published experimental values found in [48], this gives $\beta_{Rb-e-He}n_{He} \approx 1 \times 10^{-8} cm^3 / s$. Clearly, recombination with He participation dominates over direct radiative recombination.

The other recombination processes can be treated in the same way. For recombination to occur, an electron must be captured by an ion. This means the electron impact parameter must be small enough such that the Coulomb potential energy e^2/r is less than the electron thermal energy. When the electron passes the ion, the electron must interact with another particle that can receive the potential energy released at recombination commensurate with energy conservation. In the above example the third particle was a He atom. Instead, a free electron can serve the same purpose with a rate coefficient of

$$\beta_{Rb-e-e} = \frac{4\pi}{9}\sqrt{2\pi}\,\frac{e^{10}}{m_e^{\frac{1}{2}}(kT)^{\frac{9}{2}}}\ln\Omega\,, \tag{6.5}$$

where the Coulomb logarithm $\ln\Omega$ is of order unity [47,49]. The form of (6.5) can be obtained heuristically from (6.4) if we replace the He mass with the electron mass and σ_t with πr_0^2. The impact parameter $r_0 = \dfrac{e^2}{\frac{3}{2}kT}$ for our low temperature plasma is about 3×10^{-6} cm and process corresponding to (6.5) becomes comparable with (6.4) at electron densities of 10^{12} cm^{-3}.

The total recombination rate of ionized Rb atoms is described by

$$\left(\frac{dn_{ion}}{dt}\right)_{recombination} = \beta_{radiative}n_{ion}^2 + \beta_{Rb-e-He}n_{He}n_{ion}^2 + \beta_{Rb-e-e}n_{ion}^3\,. \tag{6.6}$$

6.3.6   Diffusion

Moreover, ionization results in a gradient in the number density of ions and neutral Rb atoms in the vicinity of the pump beam. Hence ionized atoms tend to

diffuse outward from the beam while neutral ground state atoms diffuse inward. The diffusion coefficient of neutral Rb in helium gas is 0.42 cm^2/s at 305 K and 1 atm [50]. Due to the simplicity of our model, we utilize the simplified description of diffusion widely used in gas discharge physics [51]. The rate of diffusive transport is $v_{dif} = D/\Lambda^2$. Λ is a characteristic length we take to be $R/2.4$ where R is the radius of the ionized region. Ambipolar diffusion describes the transport of ionized atoms. For an equilibrium plasma, the ambipolar diffusion coefficient is $D_a \approx 2D$ [51]. The net diffusion rate is described by

$$\left(\frac{dn}{dt}\right)_{diffusion} = -v_{dif}(n - n_0),$$ (6.7)

where n_0 represents the number density in the unpumped region.

6.3.7   Dimer formation

When ionization occurs in alkalis, however, dimer or trimer ions may also form via a variety of collisional channels including associative and Hornbeck-Molnar ionization [52,53]. Because the ionization potential (IP) obey IP(M)>IP(M$_2$)>IP(M$_3$), such transfers are significantly exoergic and may occur rapidly under certain conditions [38]. In comparison with energy pooling process, a relatively low rate coefficient of 3.2×10^{-13} cm^3/s at 470 K was reported for the $Rb(5p) + Rb(5p) \rightarrow Rb_2^+ + e^-$ associative ionization process in [54]. This is three orders of magnitude smaller than the corresponding energy pooling rate. Hence for our specific conditions, the effect of Rb dimers and dimer ions may be considered to be insignificant.

6.3.8   Other processes

We neglect higher order optically-induced effects including multi-photon processes and nonlinear optical effects, light forces, stimulated Penning processes and other field-assisted inelastic collisions. Other collisional processes including superelastic collision, electron impact ionization and ion-pair formation are estimated to be minor corrections and are beyond the scope of this work. Effects related to Rb-He exciplex formation are also neglected due to the low polarizability of He.

6.4   Numerical modeling

A simple rate equation model is presented here incorporating the aforementioned energy transfer processes. The three-level rate equation model used in previous studies is expanded to five levels to include the two additional population groups of interest. The energy levels of interest are the three primary lasing levels, the higher excited states including 5d, and ionized atoms. The basic kinetic processes contributing to ionization included in our model are depicted in Figure 6.3.
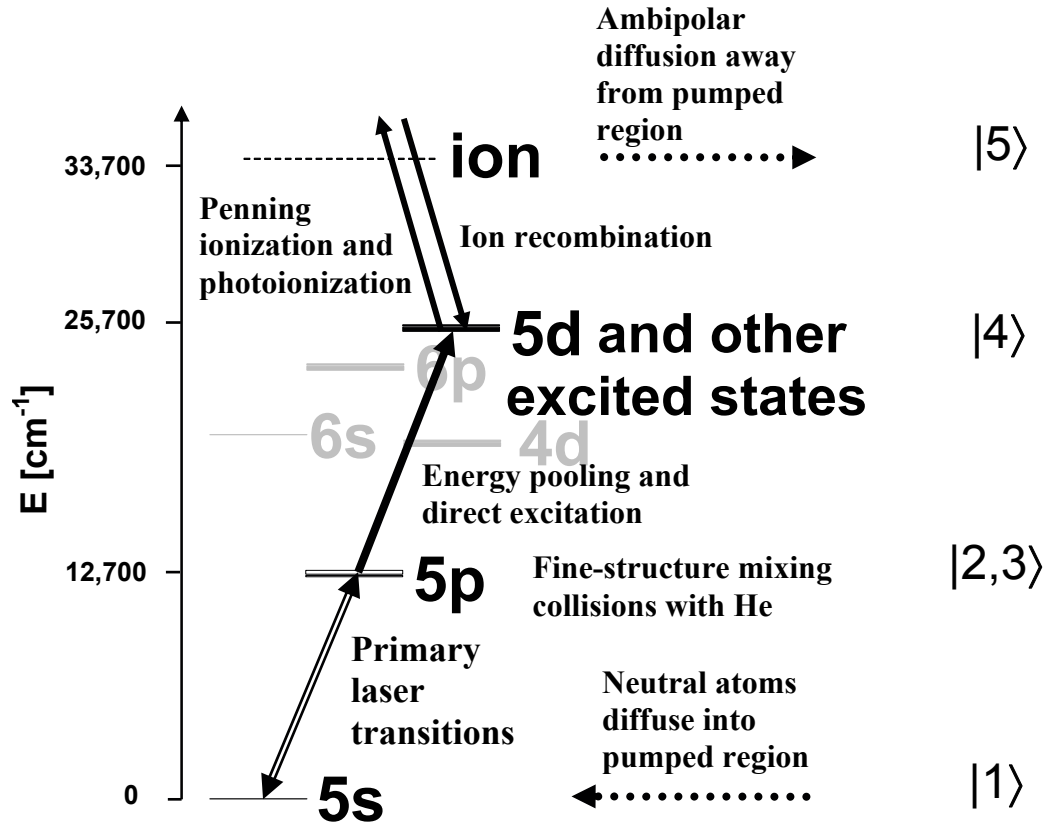
Figure 6.3: Partial energy level diagram of Rb showing the principal processes considered in numerical model. The energy splitting between the 5p fine structure levels is not explicitly shown here. The labels on the right refer to the states or subset of states considered in our model.

In our model, the number densities shall be referred to as n_i where i ranges

from 1 to 5, representing population in $5^2S_{1/2}$, $5^2P_{1/2}$, $5^2P_{3/2}$, highly excited states, and

ions respectively. The appropriate laser rate equations may be written as

$$\frac{dn_5}{dt} = W_{photoionization} + \alpha_{PI} n_4 (n_2 + n_3) - \left(\frac{dn_5}{dt}\right)_{recombination} - \left(\frac{dn_5}{dt}\right)_{diffusion}$$

$$\frac{dn_4}{dt} = W_{5P_{3/2} \to 5D} - W_{photoionization} + \alpha_{EP} n_3^2 - \alpha_{PI} n_4 (n_2 + n_3) - \frac{n_4}{\tau_3} + \left(\frac{dn_5}{dt}\right)_{recombination}$$

$$\frac{dn_3}{dt} = W_{pump} - W_{5P_{3/2} \to 5D} - \gamma_{5\,^2P_{3/2} \to 5\,^2P_{1/2}} n_3 + \gamma_{5\,^2P_{1/2} \to 5\,^2P_{3/2}} n_2 - 2\alpha_{EP} n_3^2 - \alpha_{PI} n_3 n_4 - \frac{n_3}{\tau_2} \quad (6.8)$$

$$\frac{dn_2}{dt} = -W_{laser} + \gamma_{5\,^2P_{3/2} \to 5\,^2P_{1/2}} n_3 - \gamma_{5\,^2P_{1/2} \to 5\,^2P_{3/2}} n_2 - \alpha_{PI} n_2 n_4 - \frac{n_2}{\tau_1}$$

$$\frac{dn_1}{dt} = W_{laser} - W_{pump} + \alpha_{PI} n_4 (n_2 + n_3) + \alpha_{EP} n_3^2 + \frac{n_2}{\tau_1} + \frac{n_3}{\tau_2} + \frac{n_4}{\tau_3} + \left(\frac{dn_{Rb}}{dt}\right)_{diffusion}$$

$$\frac{dP_L}{dt} = \frac{c}{2l_{cav}} \left(R_{HR} R_{OC} T_w^4 e^{2(n_2 - n_1)\sigma_1 l_{gain}} - 1 \right) P_L,$$

where the optical excitation rates are defined as,

$$W_{pump} = \frac{\eta_{mode}\eta_{del}}{l_{gain}} \int d\lambda \frac{I_P(\lambda)}{hc/\lambda} \left(1 - e^{-(n_1 - \frac{1}{2}n_3)\sigma_2(\lambda) l_{gain}}\right) \left(R_P e^{-(n_1 - \frac{1}{2}n_3)\sigma_2(\lambda) l_{gain}} + 1\right)$$

$$W_{laser} = \frac{1}{l_{gain}} \frac{I_L}{hc/\lambda_1} \frac{R_{OC}}{1 - R_{OC}} T_w \left(e^{(n_2 - n_1)\sigma_1 l_{gain}} - 1\right) \left(R_{HR} T_w^2 e^{(n_2 - n_1)\sigma_1 l_{gain}} + 1\right) \quad (6.9)$$

$$W_{photoionization} = n_4 \sigma_{photoionization} \left(\Phi_{pump} + \Phi_{laser}\right)$$

$$W_{5P_{3/2} \to 5D} = n_3 \sigma_{5P_{3/2} \to 5D}(\lambda_2) \Phi_{pump}.$$

α_{EP} and α_{PI} are the energy pooling and Penning ionization and associative ionization rates, respectively. $\beta_{Rb-e-He}$ and β_{Rb-e-e} represent the three-body recombination rate coefficients. V_L is the volume of the laser mode inside the cell. η_{mode} is the fraction of the pump light that intercepts the laser mode's cross-sectional area and thus contributes to lasing. η_{del} is the fraction of the pump power delivered from the pump excitation source to the input of the laser gain medium. $P_{pump}(\lambda)$ is the spectrally resolved pump power. Φ_{pump} and Φ_{laser} are the average pump and laser photon flux density over the gain volume. R_P represents the reflectivity of the pump

light on the high reflecting mirror after single passing the laser gain medium. T_w is the transmission efficiency through a single cell window. $\sigma_{1,2}$ is the $D_{1,2}$ line absorption cross section and $\tau_{1,2}$ the corresponding radiative lifetime. τ_3 is the effective lifetime of highly excited states. Collision induced excitation transfer rate between the fine-structure levels is represented by γ's. We make simplifying approximations that recombination processes always produce highly excited states and all excited states radiatively relax to the ground state.

Our model results show good agreement with experimental data supporting our understanding of the principal processes responsible for the transient behavior. Although our experimental conditions were changed considerably — almost 3x change in He pressure and 2x change in pump intensity and more than 5x change in Rb number density, our model was able to fit measured data in each case using the same set of physical parameters. A summary of critical parameters used in our model is found in Table 5.

Table 5: Summary of parameters used in model. Temperature T is in K. Δv_{FWHM} is the full-width of the spectral line. P_{He} is the pressure of He in atm at temperature.

Parameter	Description	Value used in model	Reference
α_{EP}	Energy pooling rate coefficient [cm^3/s]	$7.1 \times 10^{-11} T^{\frac{1}{2}}$	[40]
α_{PI}	Penning ionization rate coefficient [cm^3/s]	$3.5 \times 10^{-8} \left(\dfrac{T}{470} \right)^{\frac{1}{2}}$	[43]
$\beta_{Rb\text{-}e\text{-}He}$	Recombination rate coefficient with He as the third body [cm^6/s]	$4 \times 10^{-29} \left(\dfrac{T}{625} \right)^{-\frac{5}{2}}$	[48]
$\beta_{Rb\text{-}e\text{-}e}$	Recombination rate coefficient with e$^-$ as the third body [cm^6/s]	$3 \times 10^{-9} T^{-\frac{9}{2}}$	[49]
D	Diffusion coefficient of neutral Rb in He [cm^2/s]	$0.42 \left(\dfrac{T}{305} \right)^{\frac{3}{2}} \dfrac{1}{P_{He}}$	[50]
$\sigma_{5P_{3/2} \to 5D}(\lambda_2)$	Absorption cross section $5^2P_{3/2} \to$ 5d at λ_2=780.2 nm [cm^2]	$1.09 \times 10^{-3} \dfrac{1}{\pi} \dfrac{\frac{\Delta v_{FWHM}}{2}}{(\frac{c}{780.2nm} - \frac{c}{776nm})^2 + (\frac{\Delta v_{FWHM}}{2})^2}$	[42]
$\sigma_{photoionization}$	Photoionization cross section from 5d [cm^2]	16×10^{-18}	[44]
τ_3	Radiative lifetime of the 5d state [s]	230×10^{-9}	[42]

6.5   Discussion

The basic mechanism can be understood by considering how the excitation

transfer processes affect the lasing population. The primary levels responsible for

lasing, 5s and 5p, are rapidly intermixed by optical fields and collisionally-induced

fine-structure mixing with He. A typical optical excitation rate for the D_1 and D_2

transitions under operating condition is 10^8 transitions per ground state atom per second. In contrast, energy pooling, Penning ionization and direct excitation (5p→5d) rates are roughly 100 to 1000 times lower under the same conditions. Hence excitation transfer out of the three lowest lying states can be viewed as an adiabatic process relative to the much faster lasing process. As excited Rb atoms collide with each other, a fraction of the Rb atoms leave the primary lasing levels and become ionized. The population imbalance between the pumped and unpumped regions causes a net transport of Rb atoms out of the pumped region. Hence, ionization coupled with particle diffusion causes a decrease in the total number of Rb atoms available for lasing, resulting in a decrease in absorbed pump light and thereby causing a change in laser output. Beam deformation due to thermal lensing or gas expansion during the transient decay was not observed in agreement with the estimated slight temperature rise due to heat deposition.

The model fit in Figure 6.2(a) is markedly better than in Figure 6.2(b). We may attribute some the discrepancies to the increase of He buffer gas. Prior experimental studies from which we have acquired reported values for some of parameters in Table 5 have been performed in pure alkali environments. In the presence of many atmospheres of He gas, the interaction potential between excited alkali atoms is likely altered from that found at near vacuum. It is known that the discussed collisional excitation transfer in Rb is primarily based on dipole-dipole type of interaction at large interatomic distances [40,43]. At these distances, it is highly probable to find a He atom in between the two Rb atoms thus altering the interaction.

It has also been reported that the Rb dipole oscillator strength decreases with increasing buffer gas pressure [27,55]. Hence we expect the energy pooling and Penning ionization rates which depend heavily on the details of this interaction may also be modified in the presence of He buffer gas. The three-body recombination rates may also be affected by the presence of the high density He gas. When we reduced the pump beam diameter in Figure 6.2(c), the fit improved suggesting the overshadowing of these effects by that due to particle diffusion.

6.6   Effects on laser performance

An observation worthy of note is that while ionization-induced transient effects can strongly affect laser output, they do not represent significant energy loss channels in properly optimized systems. The drop in laser power is caused by a decrease in available population in the primary lasing levels. The decrease in laser output is accompanied by a corresponding decrease in the absorbed power by the alkali vapor. To recover optimized conditions, the vapor temperature may need to be adjusted to compensate for the amount lost due to ionization. While laser optimization may require careful considerations in light of these collisional ionization effects, we do not expect a significant impact on the intrinsic efficiency of the laser. The amount of energy used in sustaining a significant fraction of the population in the ion state is small compared to the energy converted to heat in the fine-structure mixing process. In the case of Rb, the quantum energy defect is under 2% emphasizing the minute scale of the energy expended in the creation of ions. In our Ti:sapphire pumped experiments, on the order of 10 mW of pump power is lost to the collisionally-induced

fine-structure mixing process from 1.6 W of pump power. Assuming all population that leaves the primary lasing levels uselessly radiates its energy away, the rate at which energy is being lost in populating the higher energy states and creating ions is on the order of a milliwatt. Consequently, the quantum efficiency of the Rb laser is not significantly affected.

In conclusion, ionization-induced phenomena are observed in a Rb vapor laser. These effects can be attributed to excitation transfer processes in excited alkali vapors. A simple numerical model based on published data is created to compare with experimental results. Agreement between model and experiment over a range of temperatures (Rb number densities), He buffer gas pressures and pump irradiance values support the validity of our model. While we have discussed primarily the Rb-He system, analogous excitation transfer mechanisms exist in other members of the alkali family in which the simple laser model presented here is also applicable. Further analysis is necessary to better understand the intricacies of the alkali-buffer gas system.

This chapter in part is currently being prepared for submission for publication of the material. S. S. Q. Wu, A. M. Rubenchik, S. C. Mitchell, R. J. Beach. The dissertation author was the primary investigator and author of this material.

Chapter 7   Further discussion

7.1   Optical excitation source limitations

The optical excitation source is perhaps the most critical component in the
rubidium laser. The ideal source should be monochromatic with near perfect
diffraction-limited beam quality. However as we saw in Chapter 5, typical
commercially available diode pump arrays are quite far from this ideal. Today, rapid
developments are taking place in diode laser technology that may alleviate some of the
issues we encountered.

Most diode bars and arrays operate in the wavelength region from 780 to 860
nm or between 940 and 980 nm, with the wavelengths of 808 nm (for pumping
neodymium lasers) and 940 nm (for pumping Yb:YAG) being most prominent.
Another important wavelength is 975–980 nm for pumping erbium-doped or
ytterbium-doped high-power fiber lasers and amplifiers. The Rb D_2 line at 780 nm is

at the edge of the currently available technology with only a handful of vendors

capable of making high power arrays at this wavelength. Bandgap engineering is a

technology proven effective in modifying the spectral gain characteristics of the

semiconductor material. There is no doubt that with increasing commercial and

industrial demand, advancements will make diode pump arrays at shorter wavelengths

possible.

The main obstacle limiting usage of high power diode lasers for alkali

pumping is due to their poor spatial and spectral properties. In the "fast axis"

direction, the emission comes from a very narrow region, so that the beam quality is

not far from diffraction-limited (M^2 factor not far above 1) despite the strong beam

divergence angle of typically 30–40° at FWHM. On the other hand, the "slow axis"

direction has a very wide emitting region, so that despite the much smaller divergence

angle (around 6-10°), the beam quality is very poor ($M^2 > 1000$). Significant efforts are

often required for conditioning the output of a diode bar or of multiple diode bars in

the form of a diode stack or array.

The large numerical aperture (NA) of ~0.6 for the fast axis requires high-NA

aspherical lenses for collimating the beams while preserving the beam quality. Micro-

optic fast axis collimators, containing an array of aspherical cylindrical lenses, are

often used for that purpose. The micro-optic lenses used in our experiment are one

example of such a technique. However this technique is prone to issues with stability

as we experienced in our experiments. While a single micro-lens may be placed

accurately over one diode bar, imperfections in alignment between different bars

contribute to the decrease in overall beam collimation. Moreover, as package or ambient temperature changes, the delicately mounted microlenses may begin to shift or rotate with respect to the diode bars, causing degradation in the output beam characteristics.

Diode laser arrays also tend to have imperfections with spectral control. The emission bandwidth of a diode bar typically amounts to several nanometers. In addition, there is typically a tolerance of several nanometers for the center wavelength. Several methods utilizing different kinds of external cavities with wavelength sensitive elements have been developed that significantly narrow the laser diode array linewidth. Good results have been obtained with holographic plane reflection gratings where linewidths as small as 11 GHz has been demonstrated [56]. Another approach is to use external cavities with Volume Bragg Gratings (VBG) similar to what is used in our set up. However these methods are often less than ideal. While the majority of the pump light may be under the "locked" central lobe due to optical feedback, there remains a significant portion of light that is not "locked" and forms a low lying pedestal around the central lobe. This light is not useful for excitation and can in some cases be detrimental for lasing operation. For example, as discussed in Chapter 6, they can play a role in populating undesired energy levels and increase the rate of parasitic processes in addition to thermal deposition.

Vertical-cavity surface-emitting laser (VCSEL) is another type semiconductor laser where the emitted light leaves the device in a direction perpendicular to the chip surface. The resonator is realized with two semiconductor distributed Bragg reflectors.

Between those, there is an active region with typically several quantum wells and a total thickness of only a few micrometers. The short resonator makes it easy to achieve single-frequency operation, even combined with some wavelength tunability. In addition to the high beam quality of low-power VCSEL's, an important aspect is the low beam divergence, compared with that of edge-emitting laser diodes, and the symmetric beam profile. This makes it easy to collimate the output beam with a simple lens, which does not have to have a very high numerical aperture. However, VCSEL's have been shown to possess good beam quality for fairly small mode areas and are currently limited in terms of output power. When the technological limitations restricting VCSEL's today are overcome, they may become ideal pump sources for the alkali laser as they possess the crucial spectral and spatial characteristics.

7.2   Thermal management

Generally, lasers produce more heat than light. The management and removal of this thermal energy is essential in the creation of a high average power laser. The thermally-induced index variation across the laser aperture may cause undesirable focusing or defocusing effects depending on the characteristics of the medium, degrading the output beam quality. In the alkali laser, thermal management can be accomplished by conduction and convection in the active medium or by the active flow of gas.

For a power scaled system with a preferred gain length, the required rate of gas flow depends simply on the rate of temperature rise and the allowable phase deformation. The refractive index change with temperature of 10 atm of He at

operating temperature is close to -7×10^{-7} per degree C [13]. A simplistic criterion for the maximum allowable temperature rise can be defined by stating that the resulting phase change after a single pass through the gain medium must be less than 2π. For example, this is appropriate in situations where the thermal deposition is primarily localized at the center of the pump beam. Let us assume a longitudinally pumped system with a gain length of 10 cm. The maximum temperature rise allowed based on this criterion is found to be approximately 11° C. Let us take for example a model power-scaled rubidium laser system with a rate of temperature rise of 1000° C per second. This means that the heated gas in the pumped region must be replaced with cooler gas in ~10 ms. For a laser system implementing longitudinal gas flow, where the flow direction is parallel to the optical axis, this can be achieved with a modest gas velocity of only 10 m/s. This requirement can be further relaxed if transversal gas flow is possible, requiring only ~1 m/s across an aperture size of a centimeter. However, transversal flow may be incompatible with the engineering requirement of reflective walls for effective delivery of pump light down the cell.

In power-scaled solid state lasers, the primary heat dissipation mechanism is conduction which severely limits the maximum run time of the laser. Diode-pumped alkali laser, being a type of gas laser, allows for much more effective methods for the removal of thermal energy from the laser medium. In this way, diode-pumped alkali lasers poise to be a leading candidate for directed energy applications where high average powers and good beam quality are the most critical parameters.

7.3   Coherent effects and multi-wave mixing

In Chapter 3, a rate equation model was derived from a set of atomic equations in the limit that the decoherence rate is much faster than all other time scales of interest. This remains a good approximation as long as the field intensities are low enough such that the Rabi frequencies are much lower than the decoherence rates. However, there have been numerous experiments where atomic coherent effects have manifested in alkali vapors. These atomic coherent effects are essential in the research on several effects, such as electromagnetically-induced transparency (EIT) [57,58,59], Stimulated Raman Adiabatic Passage (STIRAP) [60] and nonlinear optical effects [61]. Lasing without inversion (LWI) has been demonstrated experimentally in a V-type atomic configuration within the D_1 and D_2 lines of Rb vapor [62]. Adiabatic following and slow optical pulse propagation were also observed in rubidium vapor [63]. A helpful guide to additional literature about the roles of quantum coherence in quantum optics can be found in [64]. Remarkably, the same set of atomic equations described in Chapter 3 is applicable in describing many of these phenomena, but the equations must be carefully taken to an opposite limit, e.g. $\Delta\omega \ll \Gamma \ll \Omega$. These experiments have generally required the use of specialized lasers with extremely narrow bandwidths and vapors with very low decoherence and depolarization rates.

While we do not expect to observe any manifestations of atomic coherence in our experiments due to the high pressures of helium buffer gas leading to rapid decoherence and the use of broadband pump sources with poor optical coherence properties, it is nevertheless important to remember that this is an extremely rich field

with effects that are not well understood or recognized. In addition, the lack of evidence of classical multiwave interaction in our experiments thus far does not guarantee that those effects will not become evident at higher optical intensities. Further attention will be necessary if optical intensities are drastically increased beyond those used in our experiments.

Chapter 8   Conclusion

This work has performed an extensive conceptual and experimental study of the hydrocarbon-free rubidium laser. A semiclassical laser model is derived and utilized in experimental design and data analysis. We have demonstrated the operation of a hydrocarbon-free rubidium laser using Ti:sapphire laser and diode arrays as excitation sources. Agreement with experimental results supports the validity of our laser model and concept. Obviated is the issue of carbon formation and degradation of the vapor cell that we observed in our previous alkali laser demonstrations that used ethane as a buffer gas component to promote rapid fine-structure mixing.

Our diode-pumped experiment uses commercially available diode pump arrays with linewidths of ~0.5nm, a regime requiring only modest linewidth control with today's conventional 2-d stacks of laser diode array technology. To our knowledge,

this is the first time that a 100 W-class alkali laser has been demonstrated with ≥0.5nm bandwidth laser diode pump source. We anticipate that this approach present a new pathway to high average power lasers with good beam quality and high efficiency.

Furthermore, we exposed some physical processes which have been overlooked thus far by the alkali laser community. These processes are responsible for populating some higher lying energy states in rubidium and can manifest in changes in laser output. Extended study reveal several channels for the multistep ionization of alkali atoms. We created an expanded laser model in agreement with experiment to incorporate these effects into our laser analysis and design.

This author is grateful for the opportunity to work in close cooperation with other workers at LLNL. Moreover, this author has enjoyed acting in a central role in all aspects described in this manuscript. In the Ti:sapphire and diode-pumped demonstrations, this author was among the primary experimental researchers. The laser model described in Chapter 3 was based in part on previous work by Beach *et al* at LLNL, and vastly extended in both theoretical basis and numerical modeling capabilities. The experimental work and creation of the expanded laser model for the ionization-induced phenomena in Chapter 6 was also conducted primarily by this author. Appreciation is extended to all of LLNL for their hospitality and continuing support.

References

[1] N. V. Kravtsov, "Basic trends in the development of diode-pumped solid-state lasers", Quantum Electronics 31 (8) 661-677 (2001)

[2] P. Sprangle, A. Ting, J. Penano, R. Fischer, B. Hafizi, "Incoherent Combining and Atmospheric Propagation of High-Power Fiber Lasers for Directed-Energy Applications," Quantum Electronics, IEEE Journal of , vol.45, no.2, pp.138-148, Feb. 2009

[3] J. W. Dawson, M. J. Messerly, R. J. Beach, M. Y. Shverdin, E. A. Stappaerts, A. K. Sridharan, P. H. Pax, J. E. Heebner, C. W. Siders, C. P. J. Barty, "Analysis of the scalability of diffraction-limited fiber lasers and amplifiers to high average power," Opt. Express 16, 13240-13266 (2008)

[4] D. Hambling, "Laser Gunship Fires; 'Deniable' Strikes Ahead?", Wired, Aug 13, 2008, http://www.wired.com/dangerroom/2008/08/will-new-laser.

[5] C. Bolkcom, S. A. Hildreth, "Airborne Laser (ABL): Issues for Congress", CRS Report for Congress, 09 JUL 2007

[6] A. L. Schawlow, C. H. Townes, "Infrared and Optical Masers", Phys. Rev. 112, 1940 - 1949 (1958)

[7] S. Jacobs, G. Gould, P. Rabinowitz, "Coherent light amplification in optically pumped Cs vapor," Phys. Rev. Lett. 7(11), 415-417 (1961).

[8] P. Rabinovitz, S. Jacobs, and G. Gould, "Continuous optically pumped Cs laser," Appl. Optics 1(4), 513-516 (1962).

[9] P. Davidovits, R. Novick, "The optically pumped rubidium maser," Proceedings of the IEEE, vol.54, no.2, pp. 155-170, Feb. 1966

[10] Z. Konefal, "Observation of collision induced processes in rubidium-ethane vapour", Opt. Com. 164, 95-105 (1999).

[11] W. F. Krupke, R. J. Beach, V. K. Kanz, S. A. Payne, "Resonance transition 795nm rubidium laser", Opt. Lett. 28, no. 23, pp. 2336-2338, 2003.

[12] R. H. Page, R. J. Beach, V. K. Kanz, and W. F. Krupke, "Multimode-diode-pumped gas (alkali-vapor) laser," Opt. Lett. 31, 353-355 (2006).

[13] R. J. Beach, W. F. Krupke, V. K. Kanz, S. A. Payne, M. A. Dubinskii, and L. O. Merkle, "End-pumped continuous-wave alkali vapor lasers: experiment, model, and power scaling," J. Opt. Soc. Am. B 21, 2151-2163 (2004).

[14] T. Ehrenreich, B. Zhdanov, T. Takekoshi, S. P. Phipps, and R. J. Knize, "Diode Pumped Cesium Laser", Electronics Lett. 41, 47-48 (2005).

[15] Y. Wang, T. Kasamatsu, Y. Zheng, H. Miyajima, H. Fukuoka, S. Matsuoka, M. Niigaki, H. Kubomura, T. Hiruma, H. Kan, " Cesium vapor laser pumped by a volume-Bragg-grating coupled quasi-continuous-wave laser-diode array", Appl. Phys. Lett. 88, 141112 (2006).

[16] B. Zhdanov, C. Maes, T. Ehrenreich, A. Havko, N. Koval, T. Meeker, B. Worker, B. Flusche and R. J. Knize, "Optically Pumped Potassium Laser", Opt. Com. 270, 353-355 (2007).

[17] B. Zhdanov, A. Stooke, A. Boyadijian, A. Voci, and R. J. Knize, "17 Watts Continuous Wave Rubidium Laser," in *Conference on Lasers and Electro-Optics/Quantum Electronics and Laser Science Conference and Photonic Applications Systems Technologies*, OSA Technical Digest (CD) (Optical Society of America, 2008), paper CFW6

[18] A. Gourevitch, G. Venus, V. Smirnov, D. A. Hostutler, and L. Glebov, "Continuous wave, 30 W laser-diode bar with 10 GHz linewidth for Rb laser pumping," Opt. Lett. 33, 702-704 (2008).

[19] Daniel A. Steck, "Rubidium 85 D Line Data," available online at http://steck.us/alkalidata (revision 0.2.1, 30 April 2009).

[20] C. B. Alcock, V. P. Itkin, and M. K. Horrigan, "Vapor Pressure Equations for the Metallic Elements: 298–2500 K," Canadian Metallurgical Quarterly 23, 309 (1984).

[21] L. Krause, "Sensitized fluorescence and quenching," in *The Excited State in Chemical Physics*, J. W. McGowan, ed. (Wiley, New York, 1975), Vol. XXVIII, Chap. 4.

[22] A. Gallagher, "Rubidium and Cesium Excitation Transfer in Nearly Adiabatic Collisions with Inert Gases", Phys. Rev. 172, 88 (1968).

[23] M. D. Rotondaro, G. P. Perram, "Role of rotational-energy defect in collisional transfer between the $5\,^2P_{1/2,3/2}$ levels in rubidium", Physical Review A, 57, 4045 (1998).

[24] B. V. Zhdanov, R. J. Knize, "Advanced diode-pumped alkali lasers", Proc. SPIE 7022, 70220J (2007),

[25] L. Krause, "Collisional Excitation Transfer Between the2P½and2P3/2Levels in Alkali Atoms," Appl. Opt. 5, 1375-1382 (1966)

[26] T. J. Beahn, W. J. Condell, H. I. Mandelberg, "Excitation-Transfer Collisions between Rubidium and Helium Atoms", Phys. Rev. 141, 83 - 87 (1966)

[27] M. V. Romalis, E. Miron, and G. D. Gates, "Pressure broadening of Rb D_1 and D_2 lines by ^{3}He, ^{4}He, N_2, and Xe: Line cores and near wings", Phys. Rev. A 56, 4569–4578 (1997).

[28] W. E. Lamb, R. R. Schlicher, M. O. Scully, "Matter-field interaction in atomic physics and quantum optics", Phys. Rev. A 36, 2763 - 2772 (1987).

[29] Zoltan Fried, "Vector Potential Versus Field Intensity", Phys. Rev. A 8, 2835 - 2844 (1973).

[30] Kuo-Ho Yang, "Gauge transformations and quantum mechanics I. Gauge invariant interpretation of quantum mechanics", Annals of Physics, 101, Issue 1, p.62-96 (1976).

[31] J. R. Ackerhalt and P. W. Milonni, "Interaction Hamiltonian of quantum optics," J. Opt. Soc. Am. B 1, 116-120 (1984).

[32] P. W. Milonni, R. J. Cook, J. R. Ackerhalt, "Natural line shape", Phys. Rev. A 40, 3764 - 3768 (1989).

[33] Cohen-Tannoudji, Jacques Dupont-Roc, Gilbert Grynberg, *Atom-Photon Interactions: basic processes and applications* (John Wiley & Sons, Inc. 1992).

[34] M. O. Scully, M. S. Zubairy, *Quantum Optics* (Cambridge University Press 1997).

[35] Cohen-Tannoudji, Jacques Dupont-Roc, Gilbert Grynberg, *Photons and Atoms: Introductions to Quantum Electrodynamics* (John Wiley & Sons, Inc. 1989).

[36] T. B. Lucatorto and T. J. McIlrath, "Laser excitation and ionization of dense atomic vapors," Appl. Opt. 19, 3948-3956 (1980).

[37] R. M. Measures, P. G. Cardinal, G. W. Schinn, "A theoretical model of laser ionization of alkali vapors based on resonance saturation", J. Appl. Phys. 52, 1269 (1981).

[38] W. C. Stwalley, J. T. Bahns, "Atomic, molecular, and photonic processes in laser-induced plasmas in alkali metal vapors", Lasers and Particle Beams 11, 185-204 (1993).

[39] M. A. Mahmoud, "Kinetics of Rb_2^+ and Rb^+ formation in laser-excited rubidium vapor", Cent. Eur. J. Phys. 6(3) 530-538 (2008).

[40] L. Barbier, M. Cheret, "Energy pooling process in rubidium vapour", J. Phys. B: At. Mol. Phys. 16, 3213-3228 (1983).

[41] Y. F. Shen, K. Dai, B. X. Mu, S. Y. Wang, X. H. Cui, "Energy-Pooling Collisions in Rubidium: $5P_{3/2} + 5P_{3/2} \rightarrow 5S + (nl = 5D; 7S)$," Chinese Phys. Lett. 22, 2805-2807 (2005).

[42] D. von der Goltz, W. Hansen, J. Richter, "Experimental and Theoretical Oscillator Strengths of RbI", Phys. Scr. 30 244-248 (1984).

[43] L. Barbier, M. Cheret, "Experimental study of Penning and Hornbeck-Molnar ionisation of rubidium atoms excited in a high s or d level (5d≤nl≤11s)," J. Phys. B: At. Mol. Phys. 20, 1229-1248 (1987).

[44] M. Cheret, L. Barbier, W. Lindinger, R. Deloche, "Penning and associative ionisation of highly excited rubidium atoms," J. Phys. B: At. Mol. Phys. 15, 3463-3477 (1982).

[45] S. Wane, "Radiative recombination in rubidium", J Phys. B: At. Mol. Phys. 18, 3881-3893 (1985)

[46] A. V. Gurevich, N. D. Borisov, G. M. Milikh, *Physics of Microwave Discharges: Artificially Ionized Regions in the Atmosphere* (CRC Press, 1997).

[47] Y. B. Zel'dovich, Y. P. Raizer, *Physics of Shock Waves and High-Temperature Hydrodynamic Phenomena* (Courier Dover Publications, 2002).

[48] G. Gousset, B. Sayer, J. Berlande, "Electron-Cs^+-ion recombination in the presence of neutral helium atoms", Phys. Rev. A 16, 1070 - 1074 (1977).

[49] B. Sayer, J. C. Jeannet, J. Lozingot, J. Berlande, "Collisional and Radiative Processes in a Cesium Afterglow", Phys. Rev. A 8, 3012 - 3020 (1973).

[50] A. Fink, E. Brunner, "Optimization of continuous flow pump cells used for the production of hyperpolarized ^{129}Xe: A theoretical study", Appl. Phys. B 89, 65–71 (2007).

[51] Y. P. Raizer, *Gas Discharge Physics* (Springer-Verlag, 1991).

[52] Y. F. Shen, K. Dai, B. X. Mu, S. Y. Wang, X. H. Cui, "Energy-Pooling Collisions in Rubidium: $5P_{3/2} + 5P_{3/2} \rightarrow 5S + (nl = 5D; 7S)$," Chinese Phys. Lett. 22, 2805-2807 (2005).

[53] L. Barbier, M. Cheret, "Experimental study of Penning and Hornbeck-Molnar ionisation of rubidium atoms excited in a high s or d level ($5d \leq nl \leq 11s$)," J. Phys. B: At. Mol. Phys. 20, 1229-1248 (1987).

[54] V. M. Borodin, A. N. Klyucharev, V. Yu. Sepman, "Associative ionization of excited 52P rubidium atoms", Opt. Spektrosk. 39, 407-409 (1975).

[55] S. Y. Chen, "Broadening, Asymmetry and Shift of Rubidium Resonance Lines under Different Pressures of Helium and Argon up to 100 Atmospheres", Phys. Rev. 58, 1051 (1940).

[56] B. V. Zhdanov, T. Ehrenreich and R.J. Knize, "Narrowband external cavity laser diode array", Electronics Lett. 43, 221-222 (2007).

[57] M. Xiao, Y. Q. Li, S. Z. Jin, J. Gea-Banacloche, "Measurement of Dispersive Properties of Electromagnetically Induced Transparency in Rubidium Atoms", Phys. Rev. Lett. 74, 666 - 669 (1995)

[58] A. S. Zibrov, M. D. Lukin, L. Hollberg, D. E. Nikonov, M. O. Scully, H. G. Robinson, V. L. Velichansky, "Experimental Demonstration of Enhanced Index of Refraction via Quantum Coherence in Rb", Phys. Rev. Lett. 76, 3935 - 3938 (1996)

[59] A. J. Olson and S. K. Mayer, "Electromagnetically induced transparency in rubidium", Am. J. Phys. 77, 116 (2009),

[60] T. Cubel, B. K. Teo, V. S. Malinovsky, J. R. Guest, A. Reinhard, B. Knuffman, P. R. Berman, G. Raithel, "Coherent population transfer of ground-state atoms into Rydberg states", Phys. Rev. A 72, 023405 (2005)

[61] M. M. Kash, V. A. Sautenkov, A. S. Zibrov, L. Hollberg, G. R. Welch, M. D. Lukin, Y. Rostovtsev, E. S. Fry, M. O. Scully, "Ultraslow Group Velocity and Enhanced Nonlinear Optical Effects in a Coherently Driven Hot Atomic Gas", Phys. Rev. Lett. 82, 5229 - 5232 (1999)

[62] A. S. Zibrov, M. D. Lukin, D. E. Nikonov, L. Hollberg, M. O. Scully, V. L. Velichansky, H. G. Robinson, "Experimental Demonstration of Laser Oscillation without Population Inversion via Quantum Interference in Rb", Phys. Rev. Lett. 75, 1499 - 1502 (1995)

[63] D. Grischkowsky, "Adiabatic Following and Slow Optical Pulse Propagation in Rubidium Vapor", Phys. Rev. A 7, 2096 - 2102 (1973)

[64] J. J. Slosser and P. Meystre, "Resource Letter: CQO-1: Coherence in Quantum Optics", Am. J. Phys. 65, 275 (1997),